Isopycnal Shoaling Causes Interannual Variability in Oxygen on Isopycnals in the Subarctic Northeast Pacific

by

Ahron Cervania
A.A., College of the Redwoods, 2013
B.Sc., Humboldt State University, 2018

A Thesis Submitted in Partial Fulfillment of the
Requirements for the Degree of

MASTER OF SCIENCE

in the School of Earth and Ocean Sciences

We acknowledge and respect the lək̓ʷəŋən peoples on whose traditional territory the university stands, and the Songhees, Esquimalt, and W̱SÁNEĆ peoples whose historical relationships with the land continue to this day.

Isopycnal Shoaling Causes Interannual Variability in Oxygen on Isopycnals in the Subarctic Northeast Pacific

by

Ahron Cervania
A.A., College of the Redwoods, 2013
B.Sc., Humboldt State University, 2018

Supervisory Committee

Dr. Roberta Hamme, Supervisor
(School of Earth and Ocean Sciences)

Dr. Debby Ianson, Departmental Member
(School of Earth and Ocean Sciences)
(Fisheries and Oceans Canada, Institute of Ocean Sciences)

Dr. Jody Klymak, Departmental Member
(School of Earth and Ocean Sciences)

Dr. Tetjana Ross, Additional Member
(Fisheries and Oceans Canada, Institute of Ocean Sciences)

ABSTRACT

Over sixty years of oceanographic observations from Ocean Station Papa (OSP) in the northeast Pacific indicate the region is losing dissolved oxygen faster than the average global rate. The greatest negative trends in oxygen concentration occur on isopycnals in the upper water column (σ_θ = 26.1–26.8 kg m^{-3}) but have considerable uncertainty due to natural variability near the surface. In this thesis, I use eight Argo profiling floats equipped with oxygen optode sensors to assess the 2008—2016 interannual variability of subsurface dissolved oxygen near OSP. I developed a method to implement a time-lag correction to the optode profiles using high frequency CTD data and used reference profiles from the OSP time series to calibrate the dissolved oxygen observations. The time-lag correction markedly improves subsurface bias caused by slow optode response time. The analysis of isopycnal properties indicates that episodic shoaling of the isopycnals can cause rapid reduction of the dissolved oxygen concentration. Changes in ventilation, horizontal mixing, and water mass age were assessed and deemed unlikely drivers for the rapid O_2 loss events examined. The dissolved oxygen loss during shoaling events is linked to organic matter export, due to higher concentrations of organic matter and greater respiration rates at shallower depths. Reduced net community production during the "Blob" marine heatwave may have reduced the impact of the second shoaling event examined. Studying the natural variability of dissolved oxygen in these layers can provide context for the uncertainty in the long-term trends, as well as provide insight towards the future potential for extreme oxygen minima from the combined impacts of the long-term trend and natural variability.

Contents

List of Tables

List of Figures

ACKNOWLEDGEMENTS

I would like to thank my supervisor, Roberta Hamme, for her mentorship, gentle guidance, and inspiration during this project. I would also like to thank my committee members, Debby Ianson, Jody Klymak, and Tetjana Ross for their expertise and valuable input that helped this project develop during the course of my studies. Many thanks to Henry Bittig, Patrick Cummins, and Dana Swift for providing technical guidance and ancillary data used in this project.

This research was made possible by funding from MEOPAR through the OxyNet project. Argo data were collected and made freely available by the International Argo project and the national programs that contribute to it. The Argo Program is part of the Global Ocean Observing System. (https://doi.org/10.17882/42182#81474, https://argo.ucsd.edu, https://www.ocean-ops.org).

Chapter 1

Introduction

Dissolved oxygen (O_2) concentrations in the ocean are declining (Schmidtko et al., 2017; Ito et al., 2017). The stress imposed by this deoxygenation, combined with the impacts of ocean acidification and warming, is expected to result in harmful physiological impacts for marine species and to alter community distribution (e.g. Deutsch et al., 2015; Mccormick & Levin, 2017; Ross et al., 2020). Additionally, ocean deoxygenation can result in concurrent changes in marine biogeochemical cycling by enhancing phosphorous release from sediments (Watson et al., 2017) or altering nitrogen cycling (Bianchi et al., 2012; Babbin et al., 2015). This deoxygenation phenomenon arises from both the direct impacts of reduced solubility for O_2 and the indirect impacts of reduced circulation and enhanced biological respiration, all of which arise as a result of ocean warming under climate change (Oschlies et al., 2018). A global synthesis estimated a 2.1±0.9% decrease in the full water column O_2 inventory since 1960 (Schmidtko et al., 2017). The O_2 loss is geographically heterogenous, with some regions—such as the North Pacific—undergoing deoxygenation at a faster rate.

In this thesis, I focus on O_2 variability in the subarctic Northeast Pacific. Ocean Station Papa (Station P or OSP, 50°N, 145°W) is a key observational site for studying long-term changes within this region (Figure 1.1). Key circulatory features of the subarctic Northeast Pacific region are the North Pacific Current, Alaska Current, and Alaskan Stream (Thomson, 1981; Talley et al., 2011; Whitney et al., 2007). Together, these currents form the circulation cell of the Alaskan Gyre (AG in Figure 1.1). Waters flow into the region via the North Pacific Current, which carries a mixture of subtropical Kuroshio Current water and subpolar Oyashio Current and Western Subarctic Gyre waters. The North Pacific Current bifurcates as it approaches the west coast of North America, feeding into the Alaska Current and the California Current. The subsurface California Uncercurrent (CUC in Figure 1.1) flows along the North American margin at a depth range of 150-300 m and likewise feeds into the Alaska Current (Thomson & Krassovski, 2010). The position of the North Pacific Current can shift

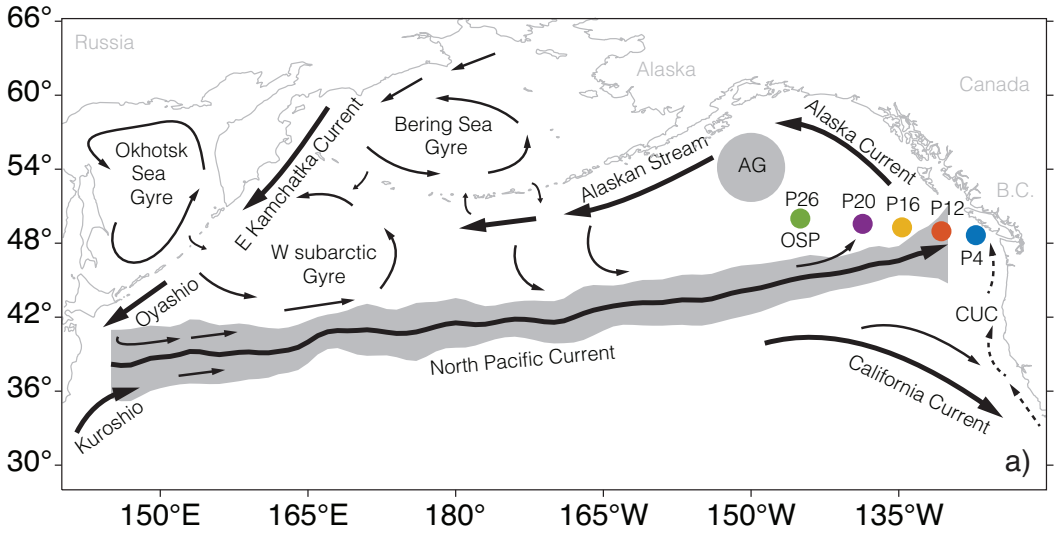

Figure 1.1: Diagram of the North Pacific Ocean showing the location of the five time series stations along Line P where the inorganic carbon system has been measured routinely. Also shown are the major near-surface currents drawn according to Talley et al. (2011), Thomson (1981), and Whitney et al. (2007)). The gray zone around the North Pacific Current (NPC) approximates seasonal and interannual excursions of the core of the NPC, calculated from gridded Argo data (Roemmich & Gilson, 2009) based on a bifurcation streamline analysis similar to Freeland and Cummins (2005). Dashed arrows represent the subsurface flow of the California Undercurrent (CUC) located over a depth range of 150–300 m (Thomson & Krassovski, 2010). Figure and caption reproduced from Figure 1a of Franco et al. (2021).

north or south seasonally and interannually. Franco et al. (2021) determined the extent of these excursions based on gridded Argo data (Roemmich & Gilson, 2009) using an analysis similar to that in Freeland and Cummins (2005) (gray zone in Figure 1.1). Due to OSP's location near the southern margin of the Alaskan Gyre, the water properties at the station can be significantly altered by these excursions of the North Pacific Current or meanders in the current (Whitney et al., 2007; Pelland et al., 2016).

O_2 measurements at OSP date back to 1956, providing one of the longest records of ocean O_2 observations in the world from which trends can be analyzed. Some of the earliest confirmation of the ocean deoxygenation phenomenon came from these data in the results of Whitney et al. (2007). Subsequent studies with additional years of data have calculated trends of reduced magnitude but which are still statistically significant (Table 1.1). Crawford and Peña (2016) state that some of the reduction in trend magnitude is due to increasing O_2 concentrations on the isopycnals at the end of their data set, highlighting the impact that O_2 variability can have on the estimation of the long-term trends. Cummins and Ross (2020) similarly find the greatest uncertainty for O_2 trends on shallower isopycnals that experience

greater interannual variability. Given the sensitivity of the trend to natural variability, future analyses of the O_2 trend at OSP may benefit from smoothing anomalous O_2 observations associated with specific mechanisms of variability that amount to short-term noise.

Table 1.1: O_2 concentration trends (μmol kg^{-1} yr^{-1}) with 95% Confidence Interval, if given, on select isopycnals at Ocean Station Papa (50°N,145°W). Note the different timespans over which the trends are calculated.

σ_θ	Whitney et al. (2007) 1956–2006	Crawford and Peña (2016) 1956–2011	Cummins and Ross (2020)[a] 1956–2018
26.3	-0.54	N/A	-0.46 (±0.20)
26.5	-0.70	-0.41 (±0.28)	-0.43 (±0.21)
26.7	-0.68	-0.50 (±0.26)	-0.51 (±0.24)
26.9	-0.60	-0.39 (±0.15)	-0.49 (±0.14)
27.0	-0.39	N/A	-0.33 (±0.17)

[a] From Fig. 11 of Cummins and Ross (2020).

O_2 concentration on the 26.5–26.7 σ_θ isopycnals at OSP is controlled by several processes, both remotely or locally (Figure 1.2). Isopycnals of $\sigma_\theta \geq 26.2$ kg m^{-3} are not observed to outcrop locally (Franco et al., 2021, Figure S3). Rather, these isopycnals only outcrop at the ocean surface in the western subarctic Pacific (Ono et al., 2001; Mecking et al., 2006), where the water takes up O_2 from the atmosphere during air-sea gas exchange and the greatest O_2 concentrations on these isopycnals are found (Figure 1.3, left). The amount of O_2 in the water parcel when it leaves the outcrop location is determined by both the area and duration of time that the isopycnal is in contact with the atmosphere (Figure 1.2, #1). Outcrop area determines the volume of water on the isopycnal which is directly ventilated; a lower volume of water being directly ventilated would result in lower average O_2 concentration on the isopycnal near the outcrop. Likewise, gas exchange between the isoypcnal and the atmosphere can only occur while they are in contact, so a reduction in the time over which the isopycnal outcrops would limit the O_2 uptake during gas exchange and result in lower average O_2 concentration on the isopycnal near the outcrop region. The maximum amount of O_2 that the isopycnal can uptake from the atmosphere is determined by the equilibrium concentration of O_2 at the water's temperature and salinity (Figure 1.2, #2). The O_2 concentration then declines as the water parcel travels with the North Pacific Current along the isopycnals towards OSP due to the cumulative respiration of organic matter. The cumulative respiration and O_2 loss that occurs during transit to OSP may increase if the age of the water parcel increases due to slower circulation (Figure 1.2, #3), allowing the water parcel to accumulate more organic matter. Additionally, the O_2 concentration observed at OSP can be altered by horizontal mixing between subpolar and subtropical waters or the horizontal displacement of the North Pacific Current (Figure 1.2, #4). Finally, the isopycnal

may shoal—move vertically to a shallower depth—which exposes it to greater organic matter concentrations and leads to greater respiration rates (Figure 1.2, #5).

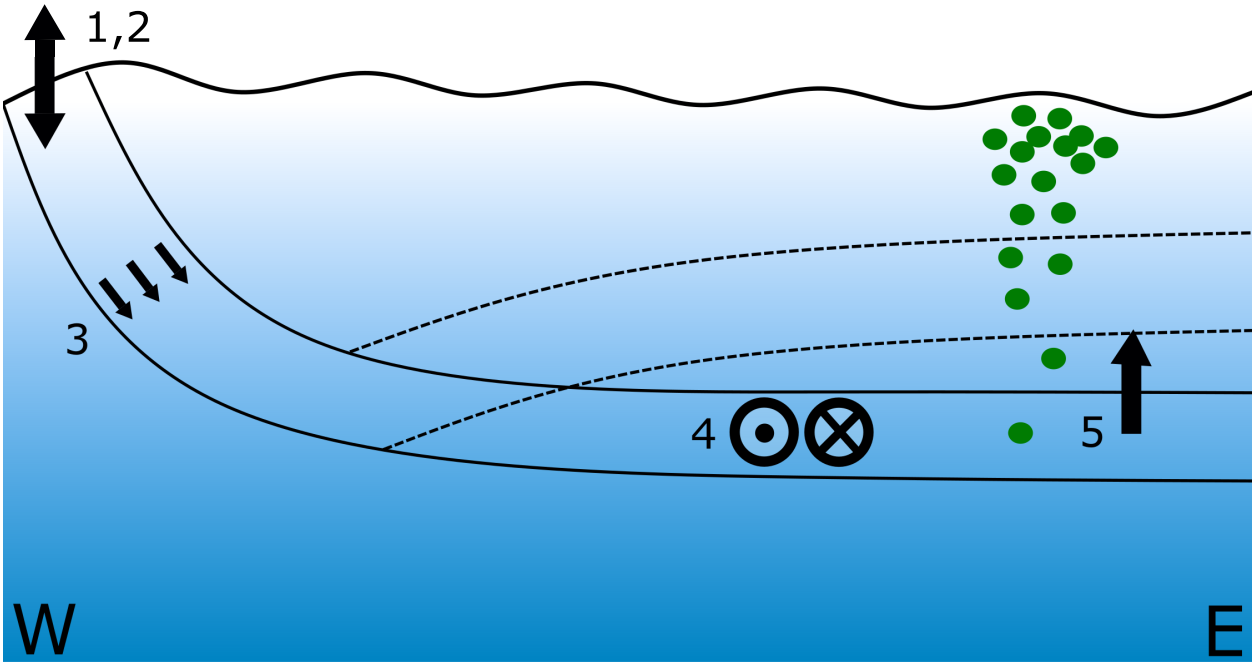

Figure 1.2: Primary drivers of natural O_2 variability on isopycnals in the northeast Pacific. 1) Area and time of isopycnal outcrop in the western Pacific; 2) Equilibrium Concentration of O_2 at outcrop; 3) Transit time/water mass age; 4) Horizontal mixing or displacement of water masses; 5) isopycnal shoaling to depths of greater organic matter export and higher respiration rates.

The implementation of optical O_2 sensors (optodes) on autonomous sensor platforms such as Argo profiling floats creates a new opportunity to examine higher frequency O_2 variability than possible with modern shipboard sampling programs. The annual contribution of O_2 profiles measured by Argo floats now exceeds that of shipboard observations and continues to grow (Johnson et al., 2015). To ensure the data received from these sensors is of sufficient quality for scientific studies, the oceanographic community has developed methods for data calibration and quality control that have greatly improved the accuracy of the optode observations. A thorough review of optode sensing principles and calibration techniques is provided by Bittig et al. (2018). Thanks to these community efforts, O_2 and other biogeochemical observations from the Argo array now have the quality and timespan to address questions of spatial and temporal scale that were previously difficult to capture (Fassbender et al., 2018; Johnson et al., 2020).

In this paper, I leverage observations from Argo floats to investigate interannual O_2 variability on isopycnals in the subarctic Northeast Pacific. I focus on the area surrounding OSP

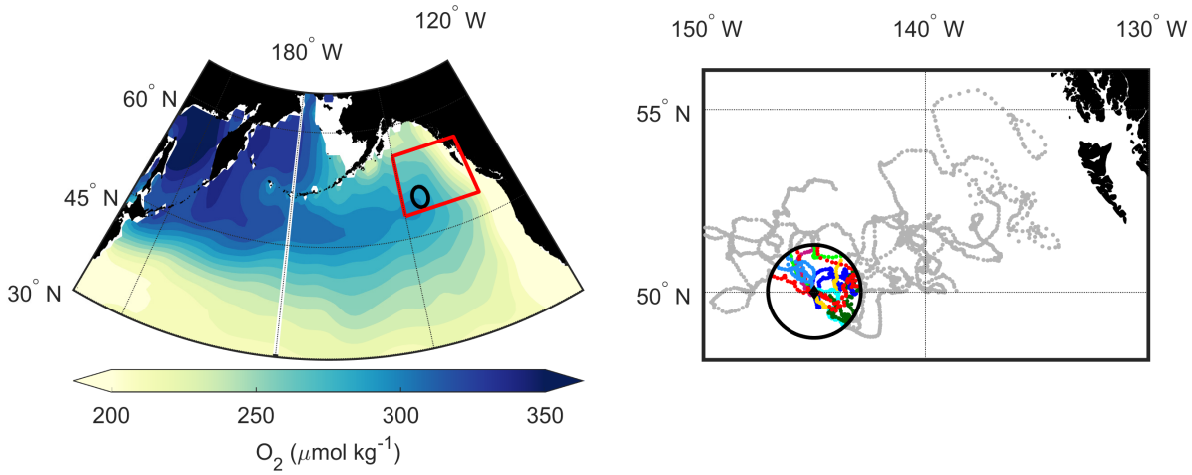

Figure 1.3: Left, Climatological O_2 distribution on $\sigma_\theta = 26.5$ kg m^{-3} in the North Pacific from the World Ocean Atlas 2018 density and O_2 data (Boyer et al., 2018; Garcia et al., 2019; Locarnini et al., 2019). Red box and black circle correspond to map limits and study area, respectively, in right panel. Right, Study area (black circle) and trajectories of Argo floats used in this study (circle markers). Colored Argo symbols are those within 150 km of OSP (black diamond marker). See legend in Figure 4.2 for float color assignments in this and later figures.

for two reasons. First, Argo floats are commonly deployed from the repeat hydrography station here. This strategy provides both a means of comparing float profiles to high-quality shipboard observations for quality control, as well as multiple Argo profiles in close geographic proximity (Figure 1.3, right) for compiling a time series of water properties. Second, the results of this investigation may supplement future analyses of O_2 variability in the OSP time series. For example, data from years in which O_2 is demonstrably low due to a local process may be excluded in future studies that seek to evaluate the deoxygenation at OSP caused by changes in ventilation at the outcrop.

In Chapter 2, I describe the data sources used in this study as well as the methodology for selecting the float data used. In Chapter 3, I describe and evaluate a method to correct bias in subsurface O_2 concentrations resulting from the slow sensor response time of optodes on Argo floats. I also update the gain calibration of the optodes using reference OSP profiles. In Chapter 4, I compile and evaluate the time series of isopycnal properties near OSP to determine the drivers of O_2 variability. I give particular attention to two episodes of isopycnal shoaling and make the argument that changes in isopycnal O_2 concentration during these episodes are primarily driven by this mechanism, rather than changes in ventilation, circulation, or water mass. I conclude in Chapter 5 with the broader relevance of the drivers of O_2 variability near OSP in the context of deoxygenation in the region.

Chapter 2

Data and Methods

2.1 Argo Floats

Argo floats included in this study were selected based on sampling location and sensor packages (Figure 2.1). First, floats with optodes deployed in the northeast Pacific (30°N–60°N, 120°W–165°W) were identified. NetCDF data files with merged salinity, temperature, pressure, and O_2 profiles for each float were accessed from the Argo Global Data Acquisition Center (GDAC) on 20 February 2021 (Argo, 2021). All raw data underwent real-time and delayed mode quality control procedures as outlined by the Argo Data Management Team (Schmechtig et al., 2016; A. Wong et al., 2021; Thierry et al., 2021). Second, floats were filtered to remove any that were not equipped with a Sea-Bird Scientific SBE 41CP CTD, which is required to apply the time-lag correction described below in Chapter 3. Finally, I limited my analysis to floats with profiles within 150 km of OSP (black circle in Figure 1.3). The radius for the study area was chosen by calculating the root mean square error between float and OSP profiles of salinity, temperature, and O_2 concentration. Within 150 km, the RMSE for all three properties was comparable regardless of distance. These selection choices led to a set of eight APEX model floats which comprised the primary dataset used in this paper. The resulting set of profiles from these eight floats provided almost continuous temporal coverage of the study area between 2008 and 2016, with each float sampling at a frequency of ∼5–10 days. Ancillary data from the SBE 41CP CTD needed for the lag correction (see Section 3.1) are recorded in the .msg files for each float profile; these files were accessed directly from the University of Washington (UW) Argo data archive (http://runt.ocean.washington.edu/argo/data/).

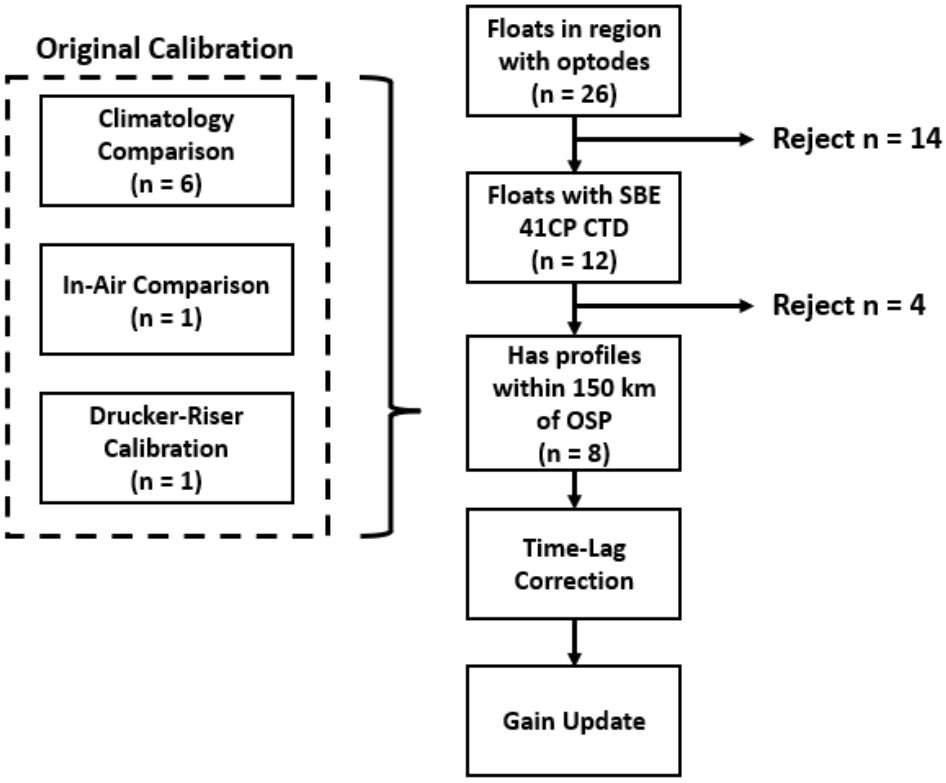

Figure 2.1: The float data selection and optode calibration workflow for this study. n indicates the number of floats in each category. Files were most recently downloaded from the Argo GDACs on 20 Feburary 2021.

2.1.1 Previous Calibration of Argo O_2 Data

Each of the eight floats used in this study underwent some calibration for the O_2 data at national DAC centers during delayed mode processing (Figure 2.1). Seven of the floats had a multiplicative gain factor applied to measured O_2 values to correct for optode drift (Table 2.1). Original optode gains and drift were determined by either comparison to an O_2 climatology following the methods of Takeshita et al. (2013) or by in-air measurements following the methods of Johnson et al. (2015). The final float did not have a gain correction method applied to the O_2 data; rather, the O_2 was recalculated from the reported optode phase and temperature measurements with a modified Stern-Volmer equation following the methods of Drucker and Riser (2016).

2.1.2 Argo Nitrate Data

In addition to the O_2 data from the Argo floats, I used any available nitrate (NO_3) data. Six of the floats used in this study had NO_3 sensors installed (Table 2.1). The sensor models were

Table 2.1: Description of Biogeochemical Sensors and Calibration for All Floats Used in This Study. $G_{original}$ is the original correction factor applied to the floats during delayed mode processing. $G_{updated}$ is the correction factor determined in this study by comparison to OSP reference profiles and applied to the floats.

WMO#	UW#	Optode Model	Original Calibration Method	$G_{original}$	$G_{updated}$	Nitrate Sensor Model
5902128	5143	Aanderaa 3830	Climatology	1.1200	1.1194	ISUS
5903274	6400	Aanderaa 3830	Climatology	1.0758[a]	1.0933	ISUS
5903405	6972	Aanderaa 3830	Climatology	1.0700	1.0745	ISUS
5903714	7601	Aanderaa 4330	Air	1.1000	1.1336	ISUS
5903743	8397	Aanderaa 4330	Modified Stern-Volmer	1.0276[b]	1.0687	N/A
5903891	6881	Aanderaa 3830	Climatology	1.1263[a]	1.1311	ISUS
5904095	8390	Aanderaa 4330	Climatology	1.0720	1.0677	N/A
5904125	7641	Aanderaa 4330	Climatology	1.1986	1.2043	SUNA

[a]Average of all G values when $G_{original}$ had drift applied.
[b]Average correction factor applied to O_2. No $G_{original}$ in this method.

either In Situ Ultraviolet Spectrophotometer (ISUS) optical sensors or Satlantic Submersible Nitrate UV Analyzers (SUNA). The NO_3 data collected by these floats were first published by Plant et al. (2016) to study net community production at OSP. They applied drift and offset corrections by comparison to World Ocean Atlas 2009 concentrations at 1000 m depth. They determined the accuracy of the NO_3 data through comparison to discrete samples from OSP. One float, WMO# 5903274, was found to have a high standard deviation for NO_3, potentially due to damage to the sensor during transport or deployment. All six floats were later used by Haskell et al. (2020) to extend the net community production analysis by two years, and to partition the contributions of particulate organic carbon and dissolved organic carbon. They chose to exclude the NO_3 data from float #5903274 due to the high standard deviation noted by Plant et al. (2016). I include these data in my study, as I only use data from this float during 2010-2011, when this float's observations matched those of other nearby floats and the OSP discrete observations (see Figure 4 of Haskell et al. (2020)). No further calibration was applied in this study.

2.2 OSP Data

The secondary dataset used in this paper is the record of discrete water samples from OSP, archived at the Institute of Ocean Sciences (IOS) operated by Fisheries and Oceans Canada. I focus on the 2008–2016 data that overlap the float observations. During this time, OSP sampling typically occurred in the months of February, June, and August. Salinity, temperature, and pressure are measured with the onboard CTD. Salinity was also measured from bottle samples at standard depths using a salinometer to confirm CTD calibration. O_2 sampling and analysis are completed at sea with an automated Winkler titration system with the modified technique of Carpenter (1965) and following the World Ocean Circulation Experiment protocols (Culberson, 1991). Data were quality checked to remove outliers and faulty data by IOS. The OSP salinity and temperature data for this time period have uncertainties of 0.002 PSU and 0.002°C, respectively (Whitney et al., 2007). The OSP O_2 data have an estimated uncertainty of 1.8 μmol kg^{-1}.

2.3 Data Processing

Profiles of water properties in the float and OSP data were processed and interpolated to isopycnal surfaces in the same manner. In situ temperature and practical salinity data were converted to conservative temperature (θ) and absolute salinity (S_A) using the TEOS-10 routines (IOC et al., 2010). The potential density (σ_θ) profiles were then calculated with the TEOS-10 routines from θ and S_A profiles.

O_2 profiles were corrected following the procedures detailed in Chapter 3. Water properties occurring at the same σ_θ (for example, within the mixed layer) were averaged to produce a single value for each unique density in the profile. O_2 and NO_3 were interpolated in density-space to the reference isopycnals with the modified Akima interpolation scheme (Akima, 1970, 1974) which maintained the profile shape better than linear interpolation when there was steep curvature in the profile such as the top and bottom of the oxycline. Salinity, temperature, and pressure, with a higher sampling frequency than O_2 and NO_3, were linearly interpolated in density-space to the isopycnals studied.

Chapter 3

Float O_2 Correction and Calibration

3.1 Time-Lag Correction

3.1.1 Time-Lag Correction Background

A remaining issue with most global Argo O_2 observations is the need for a time-lag correction (Bittig et al., 2018). Slow diffusion of O_2 from the surrounding water into the optode sensing foil (and vice versa) leads to a slow sensor response time, on the order of 70–140 seconds for standard optode foils on profiling floats (Bittig et al., 2014). The result is that the optode exhibits a lag in the observed concentrations when the float moves through high O_2 gradients faster than the time needed for the full equilibration of O_2. The magnitude of this error is significantly larger for floats with unpumped optodes (e.g. Aanderaa 3830 and 4340 model optodes like those on the floats in this study) than it is for pumped optodes (e.g. SBE 63) (Bittig & Körtzinger, 2017).

Recent work has focused on characterizing the dynamic response of the sensor and developing a time-lag correction for optodes. Bittig et al. (2014) modeled the optode response as a two-layer diffusional model and described the dependency of response time on temperature and boundary layer thickness. Once response time is determined from these parameters, they show that the corrected in situ O_2 profile can be reconstructed from the observed O_2 profile using:

$$\begin{gathered}\frac{[O_2]^{corr}_{t_{i+1}} + [O_2]^{corr}_{t_i}}{2} = \frac{1}{2b} \cdot ([O_2]^{obs}_{t_{i+1}} - a \cdot [O_2]^{obs}_{t_i}) \\ a = 1 - 2b, \quad b = (1 + 2\frac{\tau}{t_{i+1} - t_i})^{-1}\end{gathered} \tag{3.1}$$

where $[O_2]^{\mathrm{corr}}$ is the lag-corrected O_2 concentration, $[O_2]^{\mathrm{obs}}$ is the observed O_2 concentration, τ is the response time, and t is the time index for the observations. Note that the lag-

corrected O_2 values are located at the time midpoints of the observed O_2 values, which may then be interpolated back to the original observation times if desired. This formulation using the midpoints provides essentially the same result as employing the correction as a recursive equation dependent on the previous observation and averaging the results (see Appendix A.1).

The basis for applying a lag-correction to Argo data was further developed by Bittig and Körtzinger (2017), who used data from two floats to establish a relationship between the float ascent velocity and boundary layer thickness. Although the two floats exhibited slightly different ranges for boundary layer thickness at a given velocity—perhaps as a result of differences in optode orientation on the float—the response was similar (see their Figure 1). A notable feature is an apparent transition between near constant boundary layer thickness at velocities above 0.095 dbar s^{-1} (0.97 m s^{-1}) and a linear relationship at lower velocities, which may reflect the transition between turbulent and laminar flow at the optode interface. This transition point is near the typical ascent velocities for floats in the deeper water but higher than typical velocities at shallower depths where density stratification is stronger. The boundary layer thickness–velocity relationship is described by a piecewise function fit to the data of both floats:

$$l_L(\mu m) = \begin{cases} 210 - \frac{110}{0.095} \cdot |v| & |v| \leq 0.095 \text{ dbar s}^{-1} \\ 20 + \frac{60}{0.905} \cdot (1 - |v|) & |v| > 0.095 \text{ dbar s}^{-1} \end{cases} \tag{3.2}$$

where v is the ascent velocity, and l_L is the boundary layer thickness.

3.1.2 Application to Argo O_2

Applying Equation 3.1 to the Argo O_2 profile requires the response time and the time elapsed between measurements. At present, the timestamps, from which response time can be estimated, are not typically transmitted by floats to be recorded in the Argo datastream. If consecutive upcast and downcast profiles are available from a float, it is possible to determine an effective response time for a float using the direct measurements of O_2 as shown by Gordon et al. (2020). However, many floats only take upcast profiles, so the response time must be estimated by first calculating boundary layer thickness from the empirical relationship based on other floats (Equation 3.2) and then by interpolating the Bittig et al. (2014) two-layer diffusional model results to the observed temperature and calculated boundary layer thickness. In this study, I selected floats equipped with SBE 41CP CTDs from which the requisite information can be derived. The goal of the method presented here is to generate estimates of response time and measurement timestamps from the SBE 41CP CTD data so

that Equations 3.1 and 3.2 may be applied to correct the Argo O_2 observations. I will first describe the process of estimating float velocity, boundary layer thickness, response time, and relative timestamps to apply the correction to the Argo O_2 data. Following that, I describe a Monte Carlo analysis conducted to evaluate the uncertainty around the lag corrected Argo O_2 observations. Finally, I discuss the limitations of this method.

Estimating float velocity for each individual profile from the SBE 41CP CTD is a straightforward process. The CTD enters continuous profiling mode in the upper ∼1000 m of the water column, during which data are sampled every second and averaged into 2 dbar bins. The average salinity, temperature, and pressure of each bin are reported along with the number of samples per bin (n) in the .msg files transmitted directly to the float PI (Figure 3.1, first panel). Because the sampling frequency is every second in continuous profiling mode, each sample point represents one second spent within the pressure bin. The average velocity of the float through the pressure bin is therefore simply the speed (in dbar s^{-1}) required for the float to ascend 2 dbar in n seconds (Figure 3.1, second panel). I assigned the average velocity for each bin to the average pressure of the respective bin and interpolated to get the velocity at the midpoints of the O_2 observations.

From the calculated velocities, I estimate response time at the O_2 observation midpoints using the data and results from Bittig and Körtzinger (2017). First, Equation 3.2 is used to estimate boundary layer thickness from the float ascent velocity (Figure 3.1, third panel). Second, response time is determined by 2-D interpolation of the two-layer diffusion model results (Bittig & Körtzinger, 2017, supplemental material) using the temperature and boundary layer thickness at the O_2 observation midpoints (Figure 3.1, fourth panel).

Next I generate timestamps for the observations in each individual profile from that profile's n data (Figure 3.1, fifth panel). As the spacing between the average pressures reported in the .msg file sometimes exceeded 2 dbar (likely due to the rapid change in the float velocity when the float would increase buoyancy to maintain a minimum ascent velocity), I decided to assign timestamps at the average pressure of the bins, rather than at the edges that defined the 2 dbar bins. I first assign a time of $t = 0$ seconds to the average pressure for the deepest bin in the continuous profile data. Assuming that half of the time the float spends in a bin is below the average pressure of the bin (and therefore the other half of the time is above the average pressure of the bin), the time elapsed between the average pressures of two consecutive pressure bins is half the sum of time spent in both bins. A "relative timestamp" (with respect to the depth at which $t = 0$ seconds) can then be defined for the average pressure of any pressure bin as the sum of time elapsed since the first bin.

Finally, Equation 3.1 is applied to the Argo data to produce O_2 concentrations at the midpoints of the original observations. These were interpolated back to the original obser-

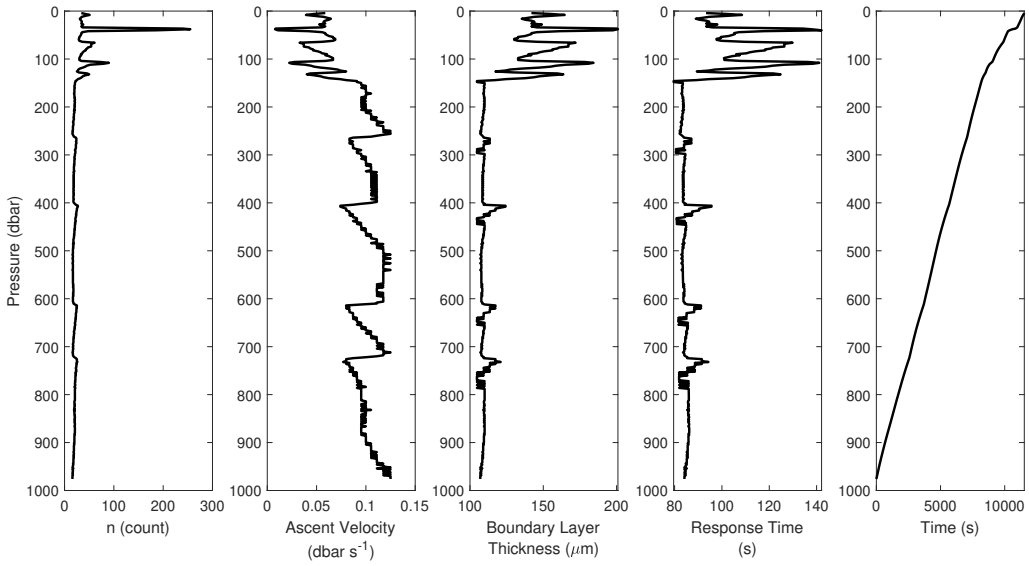

Figure 3.1: Parameters derived from n, the number of samples per 2 dbar bin, which is acquired from SBE41 CP CTD .msg files. n can directly be used to calculate ascent velocity, from which boundary layer thickness can be estimated using Equation 3.2. Response time is interpolated from the Bittig et al. (2014) diffusion model results using boundary layer thickness and observed seawater temperature. n is also used to determine a timestamp, relative to the deepest measurement in the .msg file.

vation times. Comparison to spatially- and temporally-collocated (within 150 km and 10 days) discrete samples from OSP show that the Argo data in the oxycline greatly benefit from the correction (compare orange and green curves in Figure 3.2). The peak correction magnitude tends to occur on isopycnals in the range of σ_θ = 26.0–26.5 kg m^{-3}, which is to be expected as these are the densities where the greatest O_2 gradients in depth-space occur (see Figure 4.1). However, there is considerable variability in the magnitude of the correction at any given density across all profiles and floats. For example, the standard deviation of the correction magnitude on the σ_θ = 26.5 kg m^{-3} isopycnal is 10.7 μmol kg^{-1} across all eight floats. Therefore, it would not be possible to apply a standard correction at any given density.

3.1.3 Time-Lag Correction Uncertainty

I evaluated the uncertainty of the time-lag correction using a Monte Carlo analysis. I considered uncertainty from two sources: the uncertainty of the boundary layer thickness–velocity relationship and erroneous truncation of n.

The uncertainty of the boundary layer thickness–velocity relationship stems from the

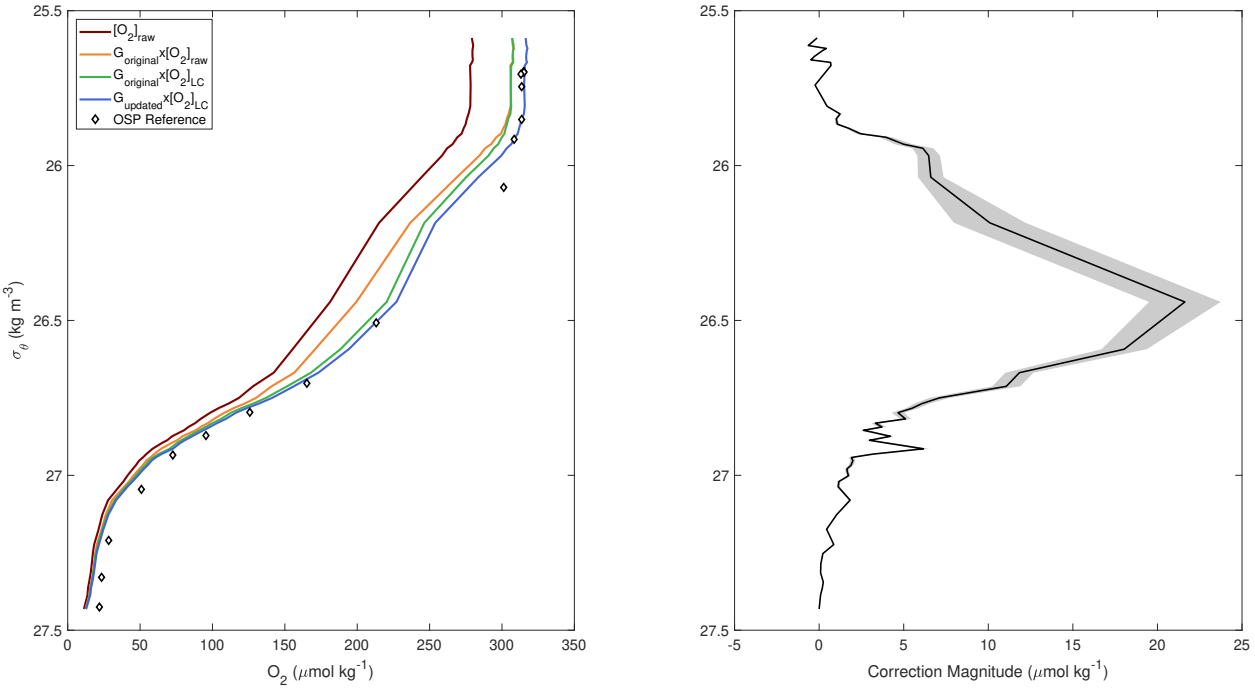

Figure 3.2: Left: Example O_2 profile from float 5903714 on June 4, 2012 compared to discrete samples from OSP on 2 June 2012 (diamonds). The locations of the profiles are approximately 77 km apart. The colored curves indicate the progressive improvement of the O_2 data from applying the original gain (maroon to orange curve), from applying the time-lag correction (orange to green curve), and then from updating the float gain (green to blue curve). Right: The mean magnitude and 1 standard deviation of the correction applied to the O_2 profile based on Equation 3.1 and the Monte Carlo simulation described in Section 3.1.3. Additional examples in Appendix A.2.

use of the piecewise linear function to estimate boundary layer thickness from velocity. As described in Section 3.1.1, Bittig and Körtzinger (2017) produced Equation 3.2 from the empirical relationship between boundary layer thickness and velocity using two floats. Although the function described the overall relationship between these variables, the data exhibited scatter around the line. This uncertainty would be carried forward into the estimates of sensor response time needed to apply the correction. To assess the uncertainty introduced by the boundary layer thickness–velocity relationship, I determined the standard deviation of the boundary layer in 0.001 dbar s^{-1} velocity bins (Figure 3.3), using the data from Bittig and Körtzinger (2017) from which Equation 3.2 is generated, and fit a 12-point moving mean.

To test the impact of the uncertainty in the boundary layer thickness–velocity relationship, I used a Monte Carlo method to adjust the boundary layer thickness over multiple trials. In each trial, I added an error to the boundary layer thickness in each of the 2 dbar pressure bins of the continuous profile data. The error was randomly selected from a Gaus-

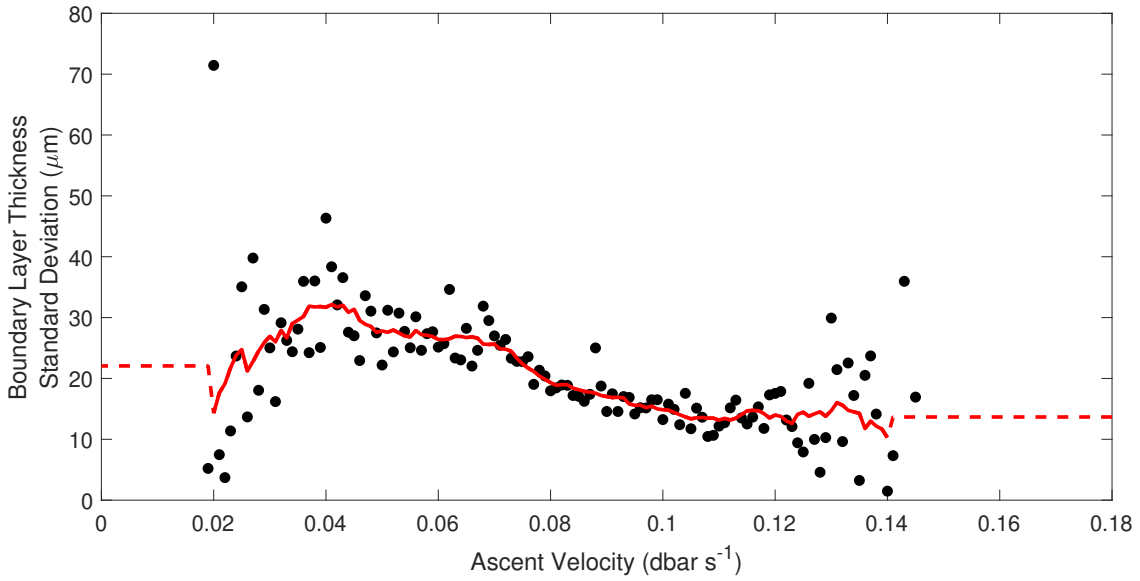

Figure 3.3: Standard deviation of the Bittig and Körtzinger (2017, their Figure 1) optode boundary layer thickness data binned in ascent velocity intervals of 0.001 dbar s^{-1}. Solid red line indicates a 12-point moving mean. Dashed red line indicates regions of low and high velocity where no data are available to calculate standard deviation. Instead, these regions have a standard deviation set at an average standard deviation of 0.02–0.03 dbar s^{-1} and 0.12–0.14 dbar s^{-1}, respectively.

sian distribution defined by a mean of 0 μm and with the standard deviation defined by the 12-point moving mean of the observed boundary layer standard deviations (red dashed line from Figure 3.3). Then, I calculated the lag-correction using the boundary layer thickness estimates with the randomized error. Across 100,000 trials, the standard deviation of the corrected O_2 profile for all σ_θ in the oxycline was small compared to the mean correction applied by the lag-correction at that density (Example shown in Figure 3.2).

The trunction of n stems from the APF9a or APF9i controller boards installed on the eight floats used in this study. These controller boards cap n at a maximum value of 255. Because the float ascent is buoyancy-driven, there were instances where the float was "trapped" in a 2 dbar bin for longer than 255 seconds by a strong density gradient, and the additional time was not recorded. This error would be carried forward into the velocity estimates (and thereafter the boundary layer thickness and response time estimates) and the relative timestamps needed to apply the correction.

To test the impact of the n truncation, I performed a separate set of Monte Carlo trials. I identified pressure bins where $n = 255$ and added 120 seconds to n. This additional time therefore carried forward into the velocity and boundary layer thickness estimates, as well as the timestamps. I prescribed uncertainty to the boundary layer thickness as

described above for 100,000 trials. The spread of uncertainty in the time-lag corrected O_2 with the added time was mostly indistinguishable from the spread generated by the uncertainty from the boundary layer thickness–velocity relationship alone (Figure 3.4). The only discernable difference is minor and occurs on isopycnals of $\sigma_\theta \leq 26.0$ kg m^{-3} where the O_2 is not rapidly changing with depth. There is no difference between the Monte Carlo simulations on the 26.3–26.7 σ_θ isopycnals I study. This result indicates that the truncation of n had little impact on the results. The minor difference between the Monte Carlo simulations is likely because the truncation error only impacts a few pressure bins in an entire profile. Additionally, despite the greater response time in these bins, the extra time allows for fuller equilibration between the optodes and the seawater.

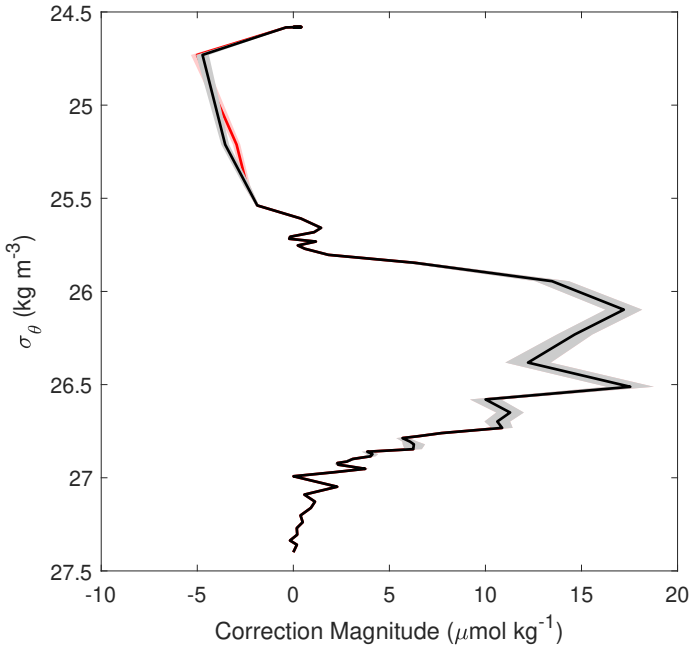

Figure 3.4: Overlapping correction magnitude and uncertainty from two Monte Carlo simulation of 100,000 trials each for a profile from 25 August 2009 from float 5902128. In the first simulation, 120 seconds were added to bins where n is truncated at the maximum value of 255 (red line). In the second simulation, no time was added to the bins with truncated n values (black line). The corrected O_2 profile can be seen in Figure A.4.

3.1.4 Limitations

I show the importance of applying a time-lag correction for studies wishing to use Argo O_2 data in the presence of a strong O_2 gradient. These methods significantly improved the accuracy of the O_2 profiles throughout the oxycline, allowing us to use these data to consider

isopycnal variability at these depths. However, limitations exist for the applicability of the method.

The first limitation is the requirement for high-frequency CTD data. The method can only be applied to floats equipped with the SBE 41CP CTD to gather the required high-frequency data. Additionally, the .msg files with the reported continuous profiling data are not part of the Argo datastream and must be located. The principal investigator(s) responsible for an individual float's data are the best contact for determining where that float's .msg file is archived.

The second limitation is that relative timestamps cannot be generated for the entire profile if floats measure deeper than the depth of the continuous profiling data ($\sim$1000 m). Without the continuous profiling data and the derived variables, a lag-correction cannot be applied to the deeper data. This limitation may be an issue for studies looking at O_2 concentrations in deep water if a high O_2 gradient exists. For this study region, the oxycline and isopycnals of interest are shallower than $\sim$400 m, and so I can apply the lag-correction at the depths where the impact of the slow sensor response time is the greatest.

The third limitation is that optode response times are treated in a uniform manner in this method but, in reality, individual optodes may respond differently. For example, Bittig et al. (2014) show that sensor configuration and orientation had a large impact on the speed dependence of response time in field experiments where an optode was deployed on a CTD frame. It is likely that similar differences in response time may occur for optodes on floats, depending on factors such as the direction of the optical window, distance from other sensors, and stalk length.

3.2 Optode Calibration With OSP Data

I checked the gain and drift during deployment for the optodes on floats used in this study by comparing the time-lag corrected Argo O_2 profiles to the OSP discrete samples. For each float profile that occurred within 150 km and 10 days of an OSP profile, I interpolated the float O_2 measurements to the σ_θ of the OSP samples. I then found the gain value which minimized the root mean square error between the OSP and float observations at densities with O_2 saturation $\geq$ 85%. This method is similar to the climatology calibration method, but using spatially- and temporally-collocated reference profiles instead. By choosing a high saturation threshold to calculate the gain, I minimize the inclusion of O_2 values from the oxycline where the lag-corrected O_2 has greater uncertainty. I also attempted a calibration using deep data at low O_2 concentrations, but the results were poor (See Appendix A.3). I found that most optodes did not have a statistically significant drift in the gain value

during deployment when comparing across all profiles sufficiently close in space and time to the discrete samples (See Appendix A.4). The three floats that did have a statistically significant drift only displayed a change of <2% yr^{-1}. This minimal drift in gain means that the optodes did not display large reductions in sensitivity to the O_2 concentrations during deployment. Therefore, I calculated a revised gain ($G_{updated}$) as the average of the individual profile gains. I found that $G_{updated}$ could be up to 3% different from $G_{original}$ and provided similar or better fit between the float and OSP samples after time-lag correction (examples shown in Figure 3.2 and Appendix A.2). For consistency of float data processing, I applied $G_{updated}$ to all eight floats used in this study.

Chapter 4

Drivers of Isopycnal O_2 Variability

The Argo data cover almost 7 continuous years of observation from late 2008 to early 2016. Figure 4.1 shows the progression of O_2 concentration for the upper 400 m of the water column during this time span, as well as the O_2 inventory for this depth range. The strong oxycline is visible and follows vertical movements of the 26.5 σ_θ isoypcnal in the water column. Additionally, the column inventory exhibits two periods of rapid decline, in 2009–2011 and again in 2014–2015. Some of the change in inventory will be due to those same vertical motions of isopycnals, which can bring deeper waters with lower O_2 content into the depth over which the inventory is integrated. However, the scale of O_2 change during these two events is quite large, suggesting a change in the balance between O_2 supply and demand in the upper water column during these periods. Because water movement in the ocean primarily occurs along isopycnals, an analysis of isopycnal properties may be able to elucidate the reason for these declines. Here, I focus on the isopycnals in the oxycline, centered on the 26.5 σ_θ isopycnal.

The compiled observations for the 26.3, 26.5, and 26.7 σ_θ isopycnals show similar trends and variability during the entire observational record considered here (Figure 4.2). Overall, O_2 concentrations are lower at the end of this observation period than at the beginning. The record is marked by several large variations in O_2 concentration. In this thesis, I focus on one of these standout features, the episode of continuous and rapidly declining O_2 concentration on the isopycnals from mid-2009 to early 2011 (first grey band in Figure 4.2), coincident with the first decline in the 0–400 m O_2 inventory. I also investigate a second, but smaller, episode of accelerated O_2 loss from January 2014 to June 2015 (second grey band in Figure 4.2), which also coincides with a decline in the 0–400 m O_2 inventory and is affected by similar dynamics as the first episode. During these events, the isopycnals experienced accelerated rates of O_2 loss between $\sim$10 and 47 times faster than the long-term trends (Table 4.1). In both of the O_2 loss episodes, the greatest losses are seen on the shallowest isopycnal,

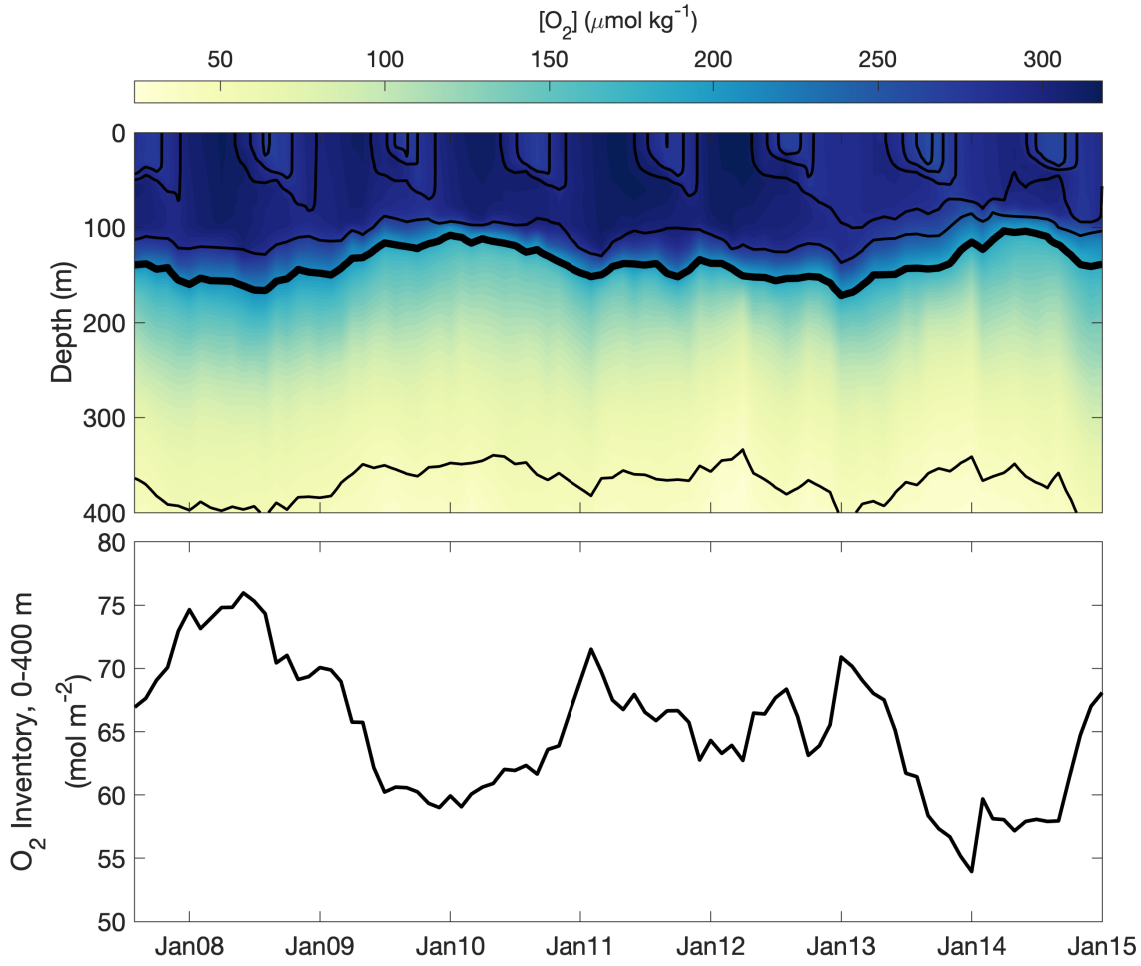

Figure 4.1: Top: Contours of monthly-averaged O_2 concentration (color) and σ_θ (black lines, spaced every 0.5 kg m^{-3} with 26.5 kg m^{-3} indicated by thick black line) in the upper 400 m of the water column from the calibrated Argo profiles in the study area. Gaps have been filled by linear interpolation. Bottom: Inventory of O_2 in the upper 400 m of the water column from the calibrated Argo profiles.

suggesting a depth-dependency to the driving mechanism. O_2 concentration on the 26.3-26.5 σ_θ isopycnals also declines in mid-2012 to early 2014, but is likely caused by a different mechanism and not accompanied by a large decrease in the 0–400 m O_2 inventory. Thus, this event is not my focus here.

I attempt to explain these episodes of rapid O_2 loss on the isopycnals by addressing the potential drivers described in Chapter 1, focusing on the 26.5 σ_θ isopycnal. First, I make the argument that shoaling of the isopycnal (Figure 1.2, #5) is the primary driver of the O_2 loss during these episodes by increasing the respiration rate. Following that, I consider and

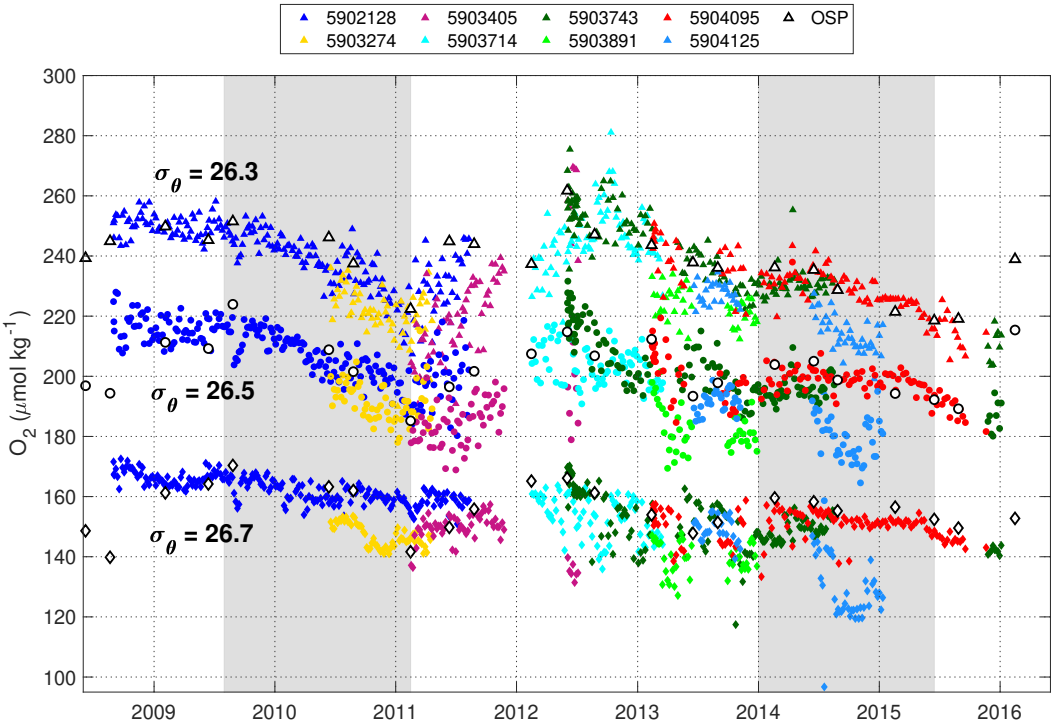

Figure 4.2: Dissolved O_2 on the 26.3 (triangle), 26.5 (circle), and 26.7 (diamond) σ_θ isopycnals from corrected Argo profiles within 150 km of OSP. Symbol fill color indicates WMO identifier for float data or OSP for bottle data. Grey shading indicate two periods of interest which are the focus of this study.

Table 4.1: Rate of O_2 loss during episodes of interest to this study. Average depth of isopycnals (m) comes from all float observations in the study area. Rate and 95% confidence interval of O_2 change determined using float O_2 observations during the periods of time indicated by grey shading in Figure 4.2.

σ_θ kg m^{-3}	Average Depth m	2009–2011 O_2 Rate μmol kg^{-1} yr^{-1}	2014–2015 O_2 Rate μmol kg^{-1} yr^{-1}
26.3	124	-21.8 ($\pm$2.4)	-12.0 ($\pm$3.6)
26.5	136	-18.6 ($\pm$2.1)	-5.2 ($\pm$4.6)
26.7	165	-10.7 ($\pm$2.1)	-5.6 ($\pm$5.1)

dismiss large contributions to the observed changes in the periods of interest from a water mass shift, increase in age, and change in air-sea equilibration at the outcrop (Figure 1.2, #4, #3, and #1–2, respectively).

4.1 Isopycnal Shoaling

I propose that vertical displacements of the isopycnals act as the driver of the observed 2008–2011 and 2014–2015 O_2 loss episodes. During both episodes, the timing of the O_2 loss is directly coincident with shoaling of the isopycnal, suggesting a link between the mechanisms. In these events, the 26.5 σ_θ isopycnal shoals from ∼170 dbar to ∼110 dbar (Figure 4.3). Displacements of similar magnitude and concurrent timing are seen on the 26.3 and 26.7 isopycnals (Figures A.22 and A.23).

Respiration rates are highest near the surface and decrease with depth as the supply of organic matter declines due to bacterial remineralization above (Figure 4.4). Therefore, as the isopycnals move closer to the surface, they should experience greater rates of O_2 consumption by respiration. OSP has been the site of numerous POC flux studies (e.g. C. Wong et al., 2002; Mackinson et al., 2015; Buesseler et al., 2020; Estapa et al., 2020). While variable, these studies all show decreasing POC flux with depth (Figure 4.4). I fit an empirical relationship based on the Martin curve (Martin et al., 1987) to these observed data, and determined that POC flux would be approximately 1.45 times larger at 110 dbar than at 170 dbar. Assuming that all else stayed constant (e.g. constant transit time and ratio of O_2 consumed per organic carbon respired), the amount of oxygen respired during transit to OSP would increase by 1.45 times as well. To compare this theoretical limit to the observed changes on the 26.5 σ_θ isopycnal, I assumed a constant equilibrium concentration of O_2 and calculated the factor by which AOU increased over each event:

$$1 - \frac{\frac{dO_2}{dt} * \Delta t}{AOU_0} \tag{4.1}$$

where $\frac{dO_2}{dt}$ is the rate of O_2 loss from Table 4.1, Δt is the duration of the event, and AOU_0 is $[O_2]_{eq}$ - $[O_2]_{observed}$ at the start of the event. The observed AOU increased by a factor of 1.31 and 1.06 for the first and second events, respectively. This simplified calculation shows that the magnitudes of the O_2 change during these events are within the theoretical limit of what could be expected if they were driven by additional respiration at these shallower depths.

The difference in the magnitude of the O_2 loss between the first and second shoaling episodes can be explained by other environmental factors. From 2014–2016, the subarctic Northeast Pacific experienced a widespread high temperature anomaly commonly referred to as “the Blob” which resulted in greater stratification across the permanent pycnocline (Bond et al., 2015). Whitney (2015) found that anomalous winds during this time reduced nutrient input to the surface layers in the transition zone between the subarctic and subtropical waters, accompanied by anomalously low surface chlorophyll in the transition zone. This

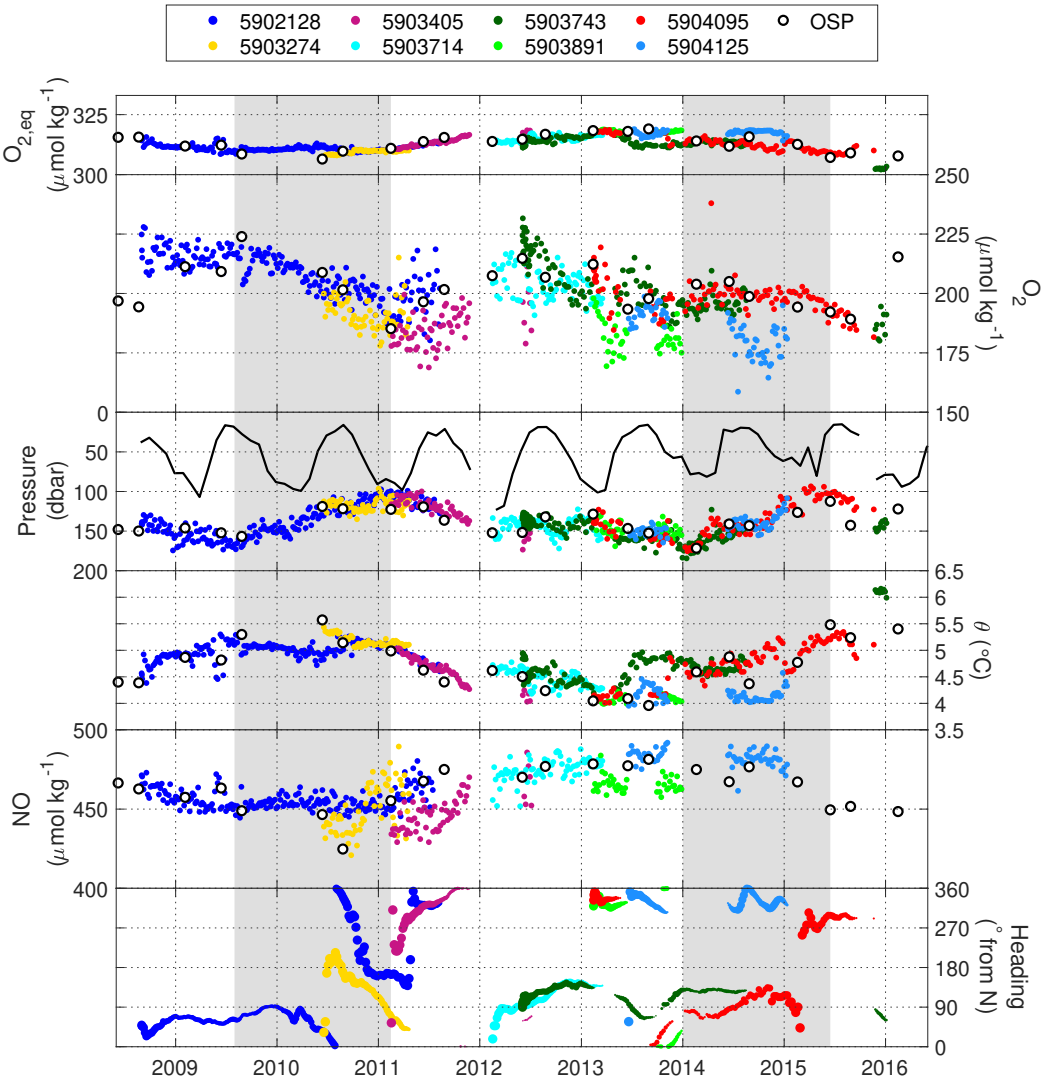

Figure 4.3: From the top, panels show the following properties on the σ_θ isopycnal: equilibrium O_2 concentration (μmol kg^{-1}), O_2 concentration (μmol kg^{-1}), pressure (dbar), conservative temperature θ (°C), and a quasi-conservative tracer NO (NO = 9.2×[NO_3]+[O_2], μmol kg^{-1}, see Whitney et al. (2007)). Bottom panel indicates the float heading from OSP (degrees, starting at 0°C due North and increasing clockwise). Float colors are the same as Figure 4.2. Black line in the pressure panel indicates the mixed layer depth, defined as the depth at which density is 0.03 kg m^{-3} greater than the density at 10 m. Marker size in the heading panel indicates relative distance from OSP, with smaller markers indicating larger distances. See Appendix A.5 for 26.3 and 26.7 σ_θ isopycnals.

result was supported by some results from Yang et al. (2018), who found that during the marine heatwave, the regional annual net community production (ANCP) in 2014 was less than half the average value (in their oxygen budget analysis, but not their DIC analysis),

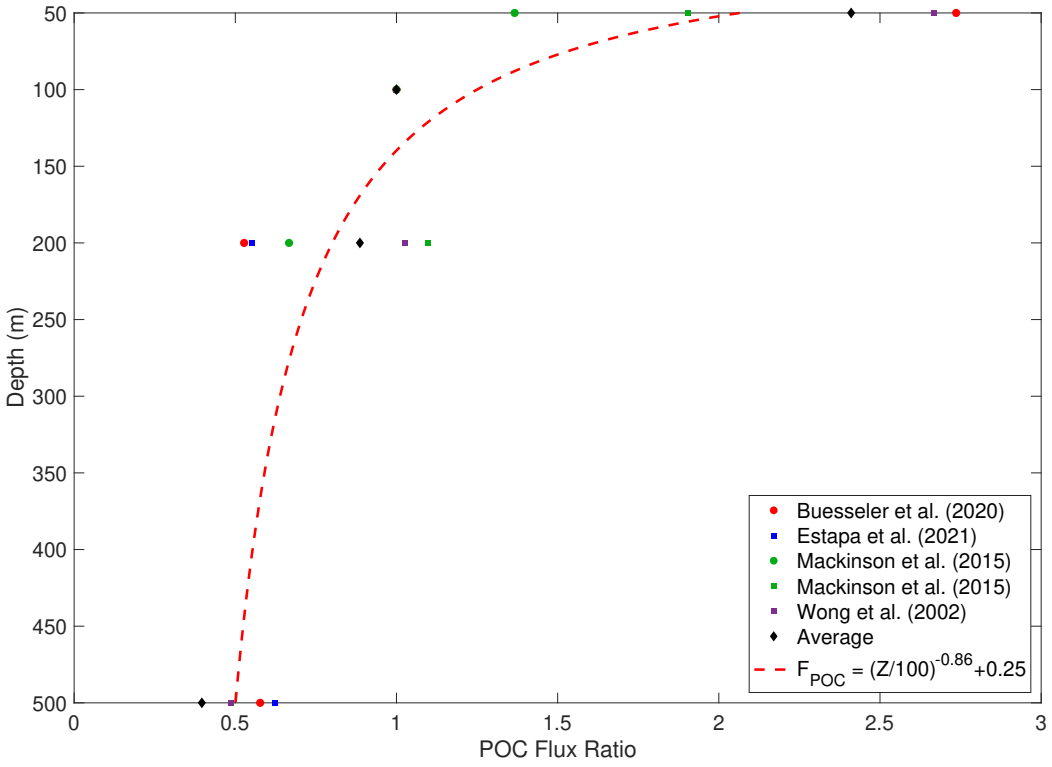

Figure 4.4: Depth profiles of the ratio of POC flux relative to the POC flux at 100 m from multiple studies. Square markers indicate studies where POC flux was determined by sediment traps, and circles are studies based on thorium-234 flux. Legend indicates original studies, but all data are transcribed from Buesseler et al. (2020). Dashed red line indicates an empirical fit to the data based on the Martin Curve (Martin et al., 1987) using a value of b = 0.86 and an offset of 0.25 (unitless).

and the phytoplankton communities shifted towards smaller picoplankton species. This combination of low productivity, smaller phytoplankton, and stronger stratification suggests that organic matter export was not able to penetrate to the deeper isopycnals at the onset of the 2014–2015 heave event, which would explain why the O_2 loss on the isopycnals denser than $\sigma_\theta = 26.3$ was not as great as expected.

However, the impacts of "the Blob" on ANCP may have been spatially heterogenous. Whitney (2015) found positive surface chlorophyll anomalies in the subarctic zone (as opposed to the the negative anomalies in the subarctic/subtropical transition zone). Float #5904125 (light blue markers, Figure 4.3) appears to sample in the cooler, fresher subarctic waters in 2014 and experiences a large drawdown in O_2, whereas floats #5903743 and 5904095 (dark green and red markers) sample east/southeast of OSP in the warmer, saltier waters that are closer to the transition zone. Importantly, 5903743 is also the float used by

Yang et al. (2018) to reach the conclusion of lower ANCP in 2014. Taken together, these details might suggest that the floats nearer to the transition zone experienced reduced O_2 demand despite the shoaling event because of the unique conditions of "the Blob", while the float further in the Alaskan Gyre experienced typical or higher O_2 demand.

Another possible contributing mechanism for the reduced O_2 demand on the 26.5 σ_θ isopycnal during "the Blob" is that warmer temperatures in the surface water could have increased the rate of respiration (Robinson, 2019). Faster respiration would result in less organic matter reaching the 26.5 σ_θ isoypcnal, regardless of whether there was a reduction in the net community production. It is not possible to distinguish between these two possible explanations for reduced O_2 demand on the isopycnal with the available information. Six of the Argo floats used in this study were not equipped with particle backscatter and chlorophyll sensors that could be used to identify the depths at which organic matter is able to penetrate.

Isopycnal shoaling may also contribute to O_2 increases on the 26.5 σ_θ isopycnal. When the isopycnal reaches its shallowest depth during the 2009–2011 shoaling event, it approaches the winter mixed layer depth (Figure 4.3). O_2 on the isopycnal began to increase at this time, potentially due to mixing with ventilated surface waters. Later, deeper winter mixed layer depths approached the slightly deeper 26.5 σ_θ isopycnal in 2012 and 2013, which may have further sustained the elevated O_2 during these years. The isopycnal and mixed layer may briefly intersect again in the winter of 2015, which may further explain the reduced O_2 loss during the second shoaling event.

Previous work has shown that the vertical displacements of isopycnals at OSP are strongly influenced by local winds. A 1-D model constructed by Cummins and Lagerloef (2002) shows that increased wind stress curl at OSP leads to more divergence of surface waters and greater Ekman suction that causes upward doming of isopycnals. Likewise, decreased wind stress curl reduces Ekman suction and leads to reduced doming of isopycnals. They found that this vertical displacement due to anomalous Ekman suction accounts for a great deal of the variability in pycnocline depth at interannual to decadal timescales, and the annual average displacements of their model had good correlation with 43 years of observations ($r = 0.77$). Figure 4.5 shows a reproduction of their model—extended to cover the study period—compared to the isopycnal pressure observations from all floats with optodes in the 150 km radius study area (i.e. not only the eight floats with the SBE 41CP). The good correlation between the model results and the observations supports the conclusion that these isopycnal displacements are largely wind-driven. As the winds are known to vary with some periodicity, I can expect these wind-driven shoaling events will continue to impact isopycnals in future observations. Cummins and Masson (2012) found that this heaving of isopycnals result in different density layers with lower or higher O_2 being present at the

standard sampling depths at OSP, and accounts for much of the O_2 variability when looking at time series at constant depths near the oxycline. This finding differs from my study since I am proposing that shoaling additionally causes O_2 declines on an isopycnal.

Although the model captures the main mode of isopycnal depth variability, other mechanisms not captured by the model can contribute to depth anomalies. The discrepancy between this model and observations in 2009 was noted by Pelland et al. (2016) who similarly reproduced the model to compare to observations from Seaglider surveys at OSP. Their results show that additional downward displacement of the isopycnal in mid-2009 was due to a meander of the North Pacific Current, which is the same as my horizontal mixing/displacement mechanism (Figure 1.2, #4). The discrepancy between model and observations from 2015 onwards was noted by Cummins and Masson (2018), who found that during this time an isopycnal depth anomaly was advected into the region with the flow of the North Pacific Current. They observed that this isopycnal depth anomaly originated west of the dateline, though the generating mechanism was not identified. The mechanism of shoaling is not of primary importance to this study if it is not due to a change in water mass, which I address in the next section. Regardless of the mechanism, the result of shoaling is that the isopycnal experiences greater respiration rates and declining O_2.

4.2 Water Mass Shift

Isopycnal properties during the two events suggest that a change in the water mass present at OSP—either due to changes in the mixing ratio of the water or a displacement of the North Pacific Current—is not the primary driver of the O_2 changes observed. The waters at OSP typically comprise a mixture of endmember water masses originating in the western subarctic Pacific (cooler, fresher, higher O_2) and the subtropical gyre (warmer, saltier, lower O_2). The contribution of these endmembers to the waters at OSP can be evaluated using both the physical properties of conservative temperature (θ) and absolute salinity (S_A), and the concentration of NO—a quasi-conservative tracer that is a linear combination of the NO_3 and O_2 concentrations. NO is formulated to be insensitive to the increase in NO_3 and decrease in O_2 caused by biological respiration (Broecker, 1974). Therefore, after leaving the ventilation region and in the absence of denitrification, the NO of a water mass is only modified by mixing. Here, I define NO as $9.2 \times [NO_3] + [O_2]$ after Whitney et al. (2007), where 9.2 is the ratio of O_2 consumption to NO_3 production during respiration in this region. For the Argo float observations near OSP, there is generally a linear relationship between NO and θ on the 26.5 σ_θ isopycnal, indicating the robustness of using these tracers to identify shifts in water mass composition (Figure 4.6). While floats 5903405 and 5903891 exhibit

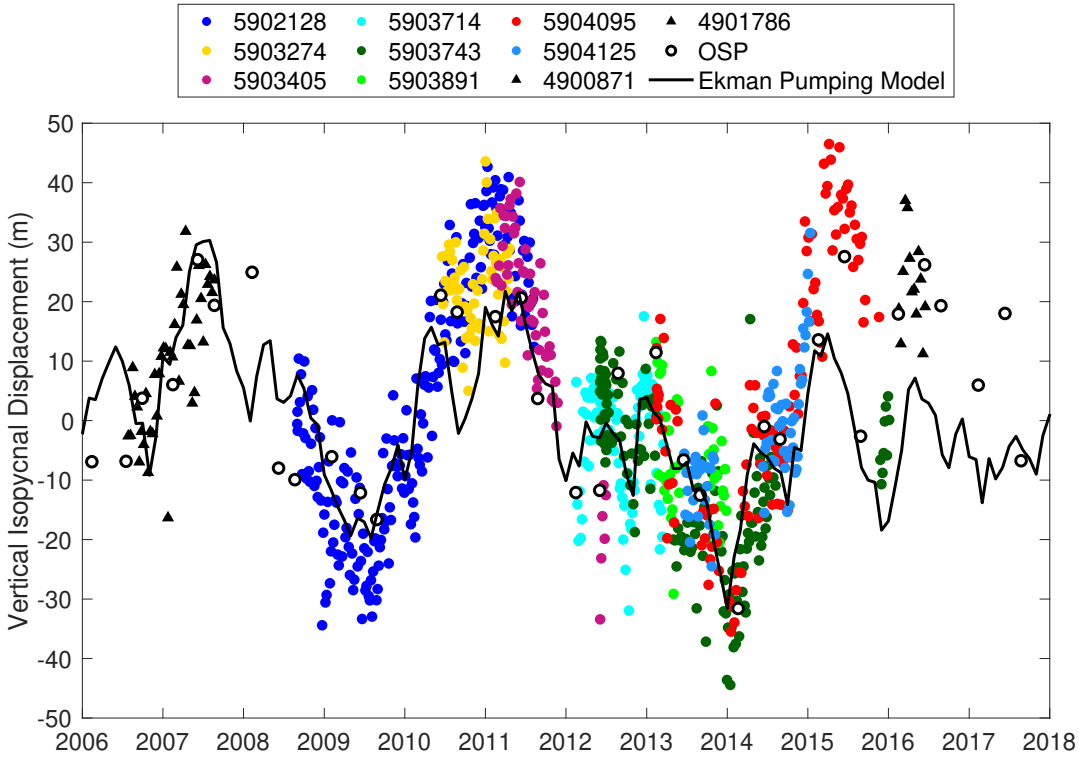

Figure 4.5: Vertical displacement anomalies for isopycnals as determined by the Cummins and Lagerloef (2002) Ekman pumping model (black line) and observations of the 26.5 σ_θ isopycnal from the OSP data (black diamond with white face) and floats used in this study (circles, with color matching those in other figures). Isopycnal displacement anomalies from two additional floats that are not included in this study but sampled within the 150 km radius are shown as well (black triangle and square). All observational data are plotted as the anomaly compared to 140 dbar, which is the approximate nominal pressure on the 26.5 σ_θ isopycnal.

lower NO values overall, they have a similar slope to the majority of the float data and the OSP discrete samples. However, a major deviation from the linear relationship is seen in the data from float 5903274. Anomalously low NO values are potentially due to a denitrification event, and are verified by the simultaneously low NO in the OSP data (Figure 4.3). The anomalously high NO values are potentially caused by O_2 increases on the isopycnal in the vicinity of the float due to contact with the mixed layer (see Section 4.4). Further investigation of the causes of these anomalous NO data are beyond the scope of my study.

From the observations of θ and NO on the isopycnal, a change in water mass does not explain the 2009–2011 event. From late 2008 to early 2016, θ displays a total range of ~4–6 °C and NO displays a total range of ~420–490 μmol kg^{-1} on the 26.5 σ_θ isopycnal. The

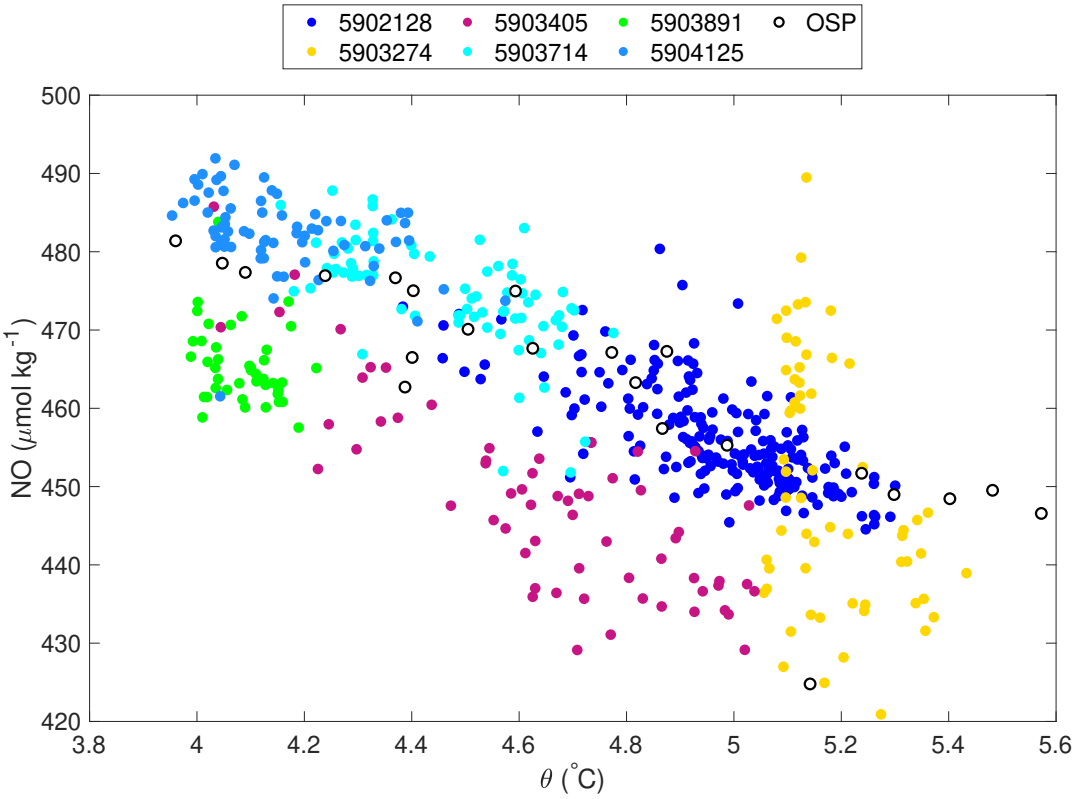

Figure 4.6: NO vs θ on the 26.5 σ_θ isopycnal from Argo profiles in study area and OSP data from June 2008–June 2016.

variability in these properties indicates that there are changes in water mass mixing ratio at OSP during the duration of the float observations, with cooler, fresher waters and higher NO when there is a greater proportion of western subarctic water at OSP and warmer, saltier waters with lower NO when there is a greater proportion of subtropical water (Whitney et al., 2007). This variability is consistent with the findings of Pelland et al. (2016), who observed warmer temperatures on the 26.5 σ_θ isopycnal at OSP when a meander of the North Pacific Current, which separates the subpolar and subtropical gyres, passed through the site. However, NO and θ on the isopycnal are relatively stable during the 2009-2011 O_2 loss event as measured by float WMO# 5902128 (dark blue markers, Figure 4.3).

The 2014–2015 event is also not likely to have been primarily driven by a shift in water mass, although this mechanism may contribute. As described above in Section 4.1, this event occurs during "the Blob" marine heatwave. Scannell et al. (2020) found that during this time, heat was able to penetrate into the subsurface waters and produce positive temperature anomalies down to the 26.3 σ_θ isopycnal. This excess heat could alter the density of subsurface waters, which would result in the isopycnal analysis following a different layer

of water than in earlier time periods. To address this potential effect, I also compiled water properties on an isohaline, a water layer with constant salinity (Figure A.24). In general, the changes on the isohaline are similar to those on the isopycnal during this event, which would indicate that my analysis is not significantly impacted by the downward propagation of heat. However, there are some differences. Notably, the O_2 change for float #5904095 appears to be reduced while the O_2 drawdown for float #5903714 increased by almost 25 μmol kg^{-1} compared to the isopycnal changes. Without additional NO data during this time, it is difficult to say exactly what role water mass change might have played in this event.

4.3 Increased Transit Time

I considered the possibility that the changing wind patterns that drive the isopycnal shoaling events could also result in O_2 losses by slowing transport of water from the ventilation region. An O_2 decline could result from either slower velocities on the isopycnal or a longer circulation pathway, leading to higher transit time and greater age of waters reaching the OSP region. Under this mechanism, there is more time for O_2 to be consumed by organic matter remineralization. While it is not possible to directly assess whether water mass age has increased using this data set, this mechanism is not likely responsible for the O_2 loss events. The shoaling of the isopycnal demonstrates that Ekman suction was anomalously high during this time. Greater Ekman suction is driven by enhanced divergence of water in the center of the gyre, leading to upward doming of isopycnals. This change in the slope of the isopycnals indicates that geostrophic currents are likewise enhanced and therefore transit time should have decreased. This suggestion is supported by the results of Onishi (2001), who found that geostrophic velocity and volume transports in the Subarctic Current/North Pacific Current increased during periods of gyre upwelling. To produce the O_2 loss observed in the 2009–2011 event, the circulation pathway would have had to greatly increase if velocities were enhanced (rather than being slower or stable). Such a change in large-scale circulation is unlikely to have occurred. Furthermore, I would expect that if this mechanism were to have caused the first O_2 loss event, then I should see a similar magnitude of O_2 loss in the second event.

4.4 Ventilation Efficiency

I finally consider the possibility of a decrease in O_2 supply at the ventilation region. The entire June 2008–January 2016 record of equilibrium concentration of O_2 on the 26.5 σ_θ isopycnal exhibited a range of 17.0 μmol kg^{-1} (Figure 4.3). During the first event, the

equilibrium concentration only had a range of 5.5 μmol kg^{-1} and only a slight trend of -0.5 μmol kg^{-1} yr^{-1}. Therefore, the possible solubility-driven effect on air-sea gas exchange was small in contrast to the 32.0 μmol kg^{-1} decrease in average O_2 concentration during the first event. This discrepancy in magnitude means that a change in supply from ventilation for the first event would primarily have to originate from decreased time or area over which the isopycnals ventilate.

Two pieces of evidence suggest that there was no significant change in outcrop time or area related to the first episode. First, an evaluation of the monthly-averaged mixed layer depth in the Oyashio region from July 2002 to June 2006 found that the winter maximum exceeded 200 m depth in all years except for the 2005–2006 winter season (Kako & Kubota, 2007). Shallower winter mixing would reduce ventilation of deeper isopycnals, and that signal would be advected to the eastern Pacific. Given the approximately 7 year transit time for waters advecting to OSP from the ventilation region (Ueno & Yasuda, 2003), a reduction in O_2 supply from the 2005–2006 winter season would be evident in 2012 or 2013, rather than the 2009–2011 change that I see. Second, a change in the ventilation should be evident in NO. Due to the formulation of NO, a decrease in ventilation would necessitate a decrease in NO unless there was a compensating increase in NO_3 at the ratio of 9.2. However, while reduced atmospheric contact limits O_2 uptake via gas exchange, NO_3 is not impacted by gas exchange and therefore is not dependent on the the outcrop time or area. This decoupling of NO_3 and O_2 concentrations via air-sea gas exchange suggests that it isn't possible for NO_3 to increase as a result of reduced atmospheric contact, and even more unlikely that it would do so at the proper ratio to maintain a constant NO. Since NO remains approximately constant during the first O_2 loss event, decreased ventilation efficiency is an unlikely contributor to these events.

However, changes in ventilation efficiency may have contributed to the difference between the first and second event. The change in average O_2 concentration during the second event—estimated as the difference between average concentration in January 2014 and June 2015—was only a decrease of 3.6 μmol kg^{-1}. This change is comparable in magnitude to the 9.7 μmol kg^{-1} range and trend of -1.5 μmol kg^{-1} yr^{-1} of the O_2 equilibrium concentration during the second event. It is possible that this reduction in equilibrium concentration could have resulted in less O_2 uptake at the outcrop area before the waters subducted. Furthermore, there are limited NO data available for the second episode and so this mechanism cannot be ruled out.

Chapter 5

Conclusion

Biogeochemical sensors on Argo floats and other autonomous sensing platforms continue to expand the coverage of oceanographic observations to include finer temporal scales over greater spatial scales. These data can provide valuable context to supplement the interpretation of records from oceanographic time series sites which span a longer time period but with lower temporal resolution. However, high-quality data from shipboard observations are necessary for rigorous quality control of data obtained by these platforms. In this study, I demonstrated these concepts by applying corrections to Argo O_2 data in the subarctic Northeast Pacific and validating the results against collocated discrete observations from the Ocean Station Papa time series.

The results of the data corrections indicate the importance of applying both a time-lag and gain correction when using Argo data to study subsurface O_2. Without the time-lag correction, Argo O_2 profiles in the study region exhibit a bias towards lower concentrations throughout the depths of the oxycline. The floats used in this study showed corrections on the order of 20–30 μmol kg^{-1} on the 26.5 σ_θ isopycnal. Some bias is maintained until the float reaches the mixed layer. Likewise, it is well documented in the literature that sensor drift prior to float deployment results in lower O_2 concentrations if not corrected with a gain factor. I found that for the floats used in this study, the observations benefited more from a gain calculated by comparison to the Ocean Station Papa discrete samples rather than climatological profiles or in-air measurements.

Time series of water properties on isopycnals from the float and discrete samples were used to identify a relationship linking changes in isopycnal depth and O_2 concentration. During two isopycnal shoaling events, O_2 was rapidly depleted, as would be expected due to greater supply of organic matter to the isopycnal from the euphotic zone driving enhanced bacterial respiration. The rate of O_2 loss during these events was between $\sim$10–47 times larger than the long-term trend. The general stability of $[O_2]_{eq}$, NO, and θ on the isopycnal

suggests that other mechanisms cannot explain the rapid O_2 loss during the first of these events. However, the limited data during the second event means I cannot rule out the potential that other driving mechanisms contributed to the O_2 loss in 2014–2015.

Despite the episodic nature of these events, they have relevance when considering the long-term O_2 conditions of the North Pacific. This region has already been identified to be experiencing long-term deoxygenation at a faster rate than the global average, but the trend estimates are sensitive to the natural variability in the region. By causing a rapid reduction in the O_2 on an isopycnal, shoaling events add noise onto the long-term deoxygenation signal. Smoothing out these events with moving mean averages covering several years of data may improve future long-term trend analyses to better forecast the ecosystem state of the region in coming years. As the mean O_2 concentrations continue to decline due to ocean deoxygenation, the potential for these events to cause a rapid onset of an extreme O_2 minima on an isopycnal increases, and the vertical displacement of the isopycnals can bring the minima to depths that will impact marine life.

Appendix A

Additional Information

A.1 Lag-Correction Recursive Equation Comparison

Equation 3.1 can also be formulated as a recursive filter, so that the value at any point is calculated as a function of the previous value. In other words, both sides of the equation would be multiplied by 2 and $[O_2]_{t_i}^{corr}$ would be moved to the right-hand side of the equation. This formulation was also presented in Bittig et al. (2014)[their Equation 35], with the warning that this method results in strong oscillations due to sensor errors and that additional averaging would be required. They suggest instead their Equation 36, which is the midpoint formulation used in this thesis. Here, I compare the results using both methods.

Overall, the results are indistinguishable from each other (Figure A.1). We see the strong oscillations produced by the recursive filter formulation, producing a jagged O_2 profile. However, averaging consecutive pairs of the resulting O_2 profile and placing that value at the midpoint produces a profile that very closely follows that of the midpoint correction. As these results are indistinguishable and the midpoint formulation removes the requirement for an additional averaging step, I use this method throughout the thesis.

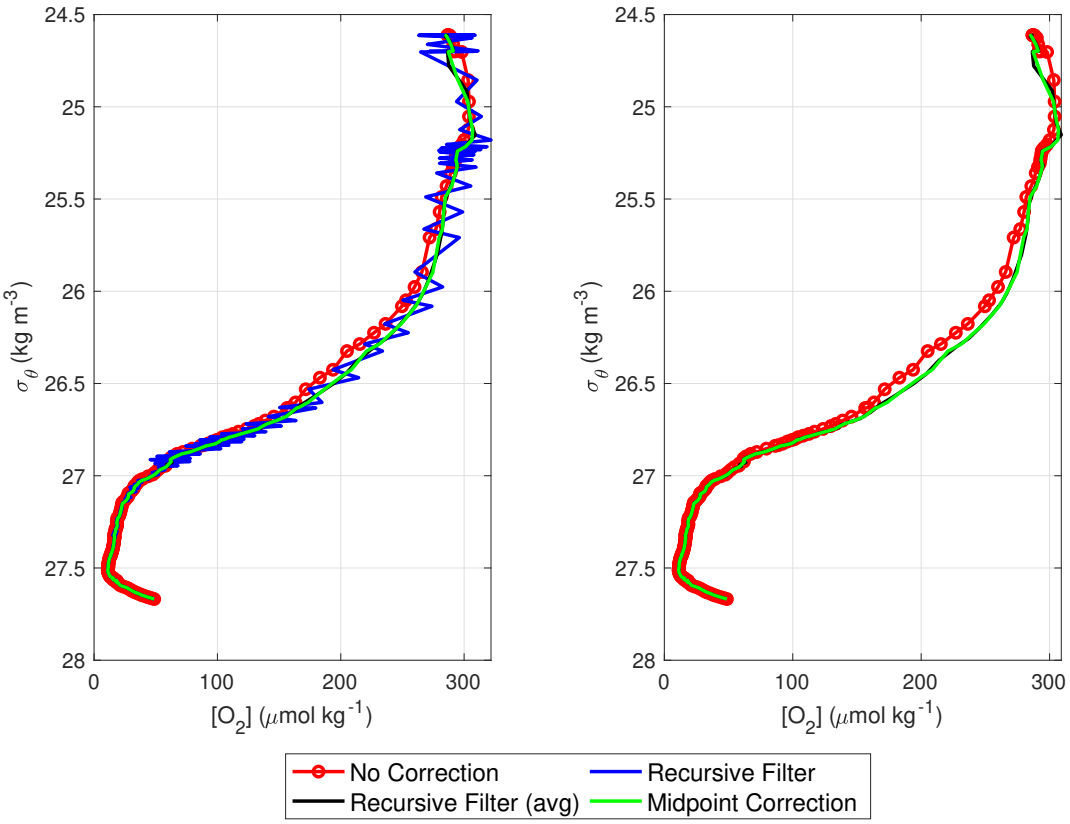

Figure A.1: Left: A comparison of a single Argo O_2 profile with no correction (red line with markers), with lag-correction using a recursive filter formulation (blue line), and with lag-correction using the midpoint formulation used in this thesis (green line). Additionally shown is the profile that results from averaging consecutive pairs of lag-corrected data from the recursive formula (black). Right: The same as the left panel, but with blue line removed for clarity.

A.2 Additional Correction Examples

This section of the Appendix is divided into subsections for each of the eight lag-corrected floats used in the study. Each subsection contains examples of the float's corrected O_2 profiles and the uncertainty of the lag-correction. Example profiles are all from within 10 days and 150 km of a reference profile at OSP, which is also shown in the left panel.

A.2.1 WMO# 5902128

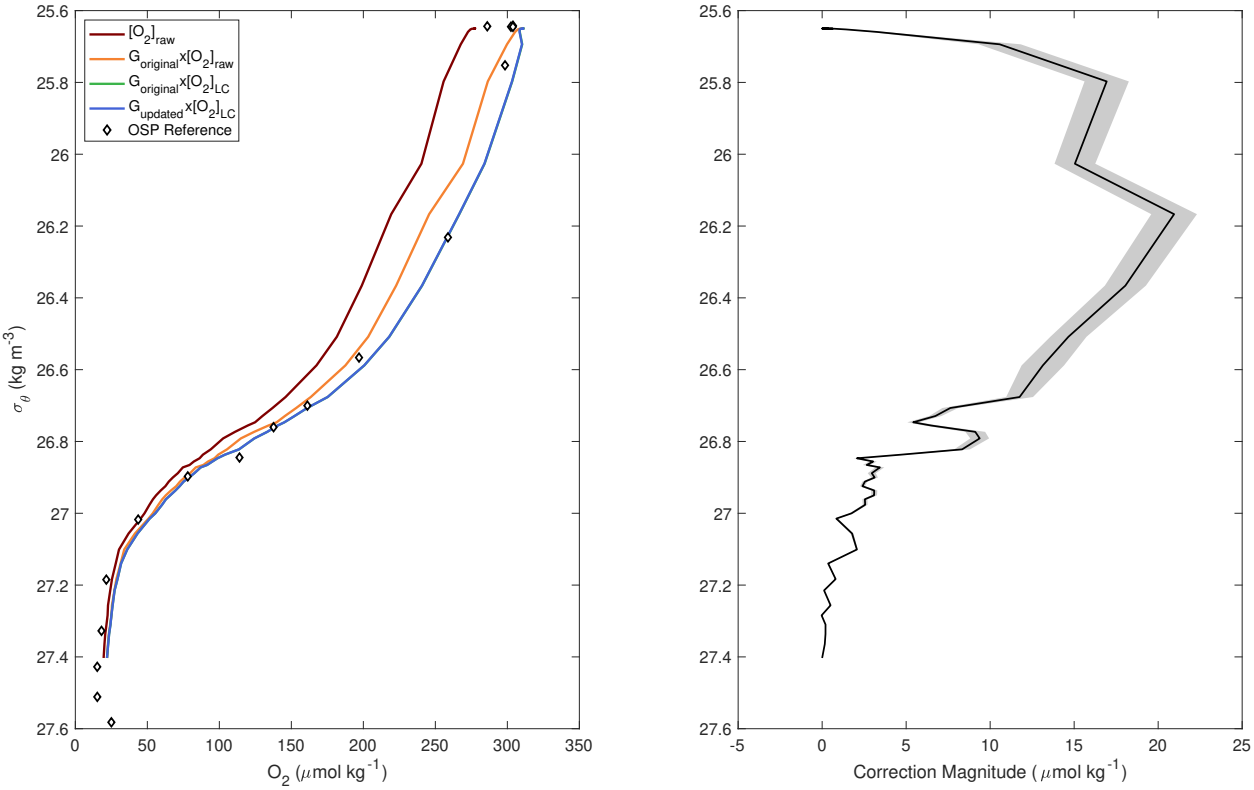

Figure A.2: Same as Figure 3.2 but for float # 5902128 on February 5, 2009. OSP reference profile is from February 4, 2009. Note that for this float, $G_{original}$ and $G_{updated}$ are very close (<0.1% difference), so the green and blue lines mostly overlap.

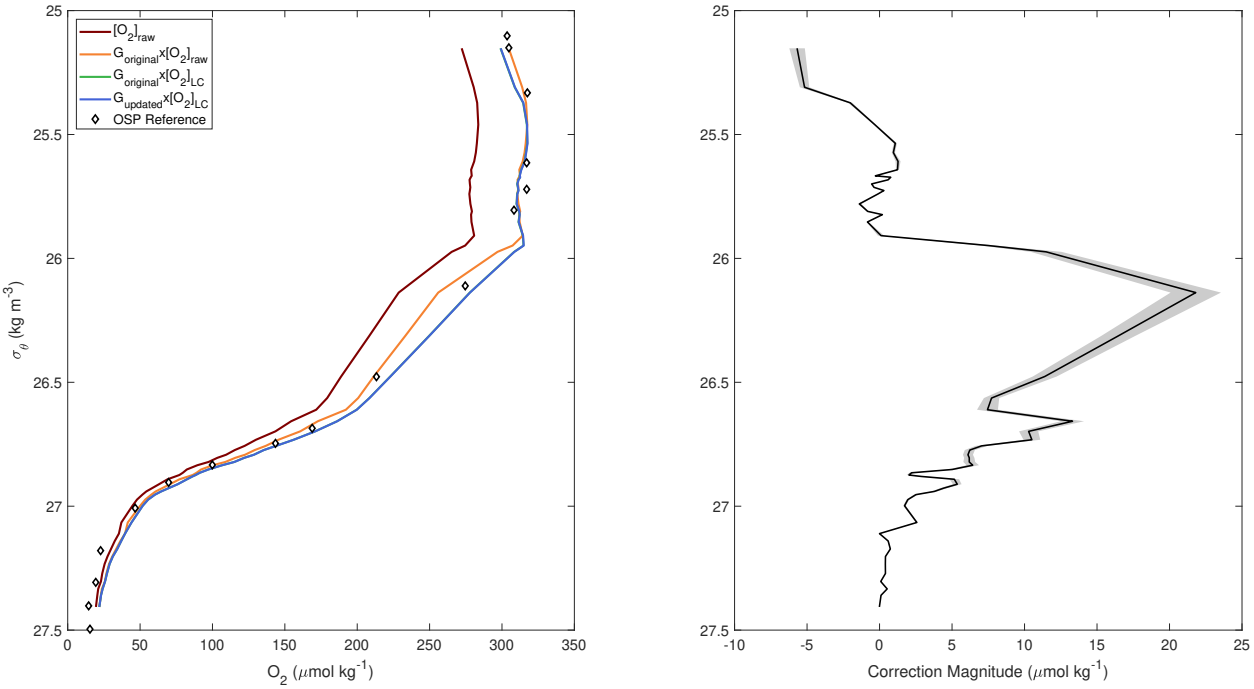

Figure A.3: Same as Figure 3.2 but for float # 5902128 on June 16, 2009. OSP reference profile is from June 14, 2009. Note that for this float, $G_{original}$ and $G_{updated}$ are very close (<0.1% difference), so the green and blue lines mostly overlap.

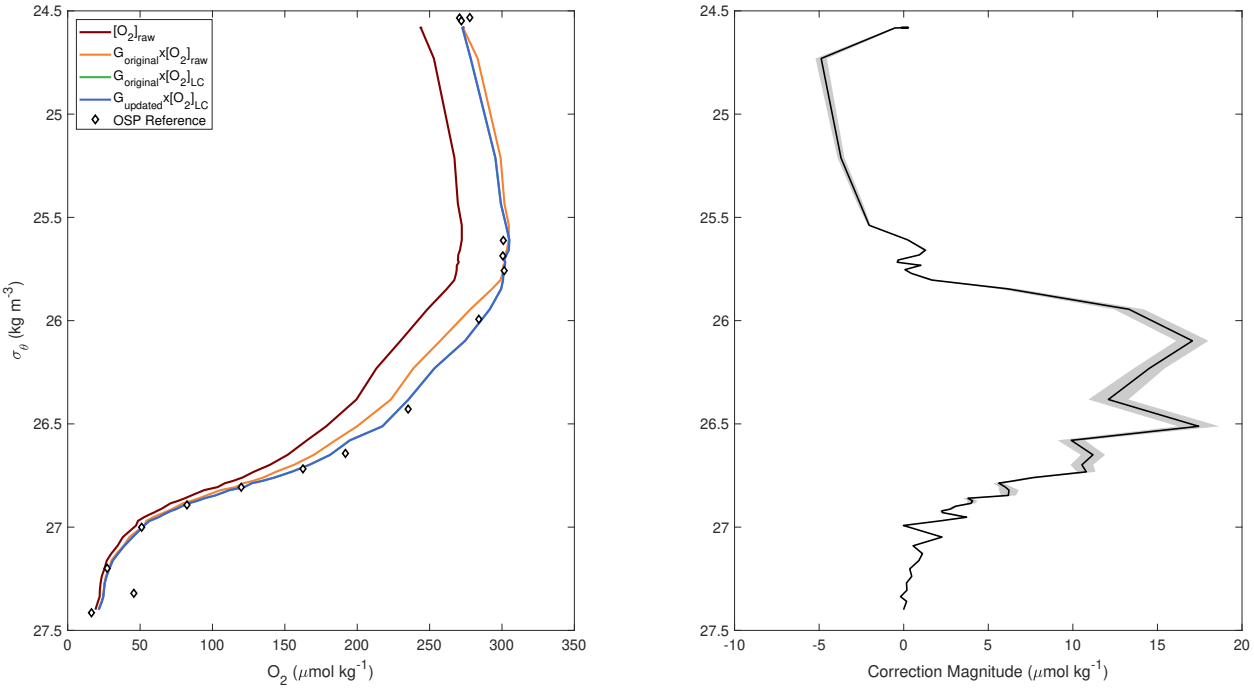

Figure A.4: Same as Figure 3.2 but for float # 5902128 on August 25, 2009. OSP reference profile is from August 27, 2009. Note that for this float, $G_{original}$ and $G_{updated}$ are very close (<0.1% difference), so the green and blue lines mostly overlap.

A.2.2 WMO# 5903274

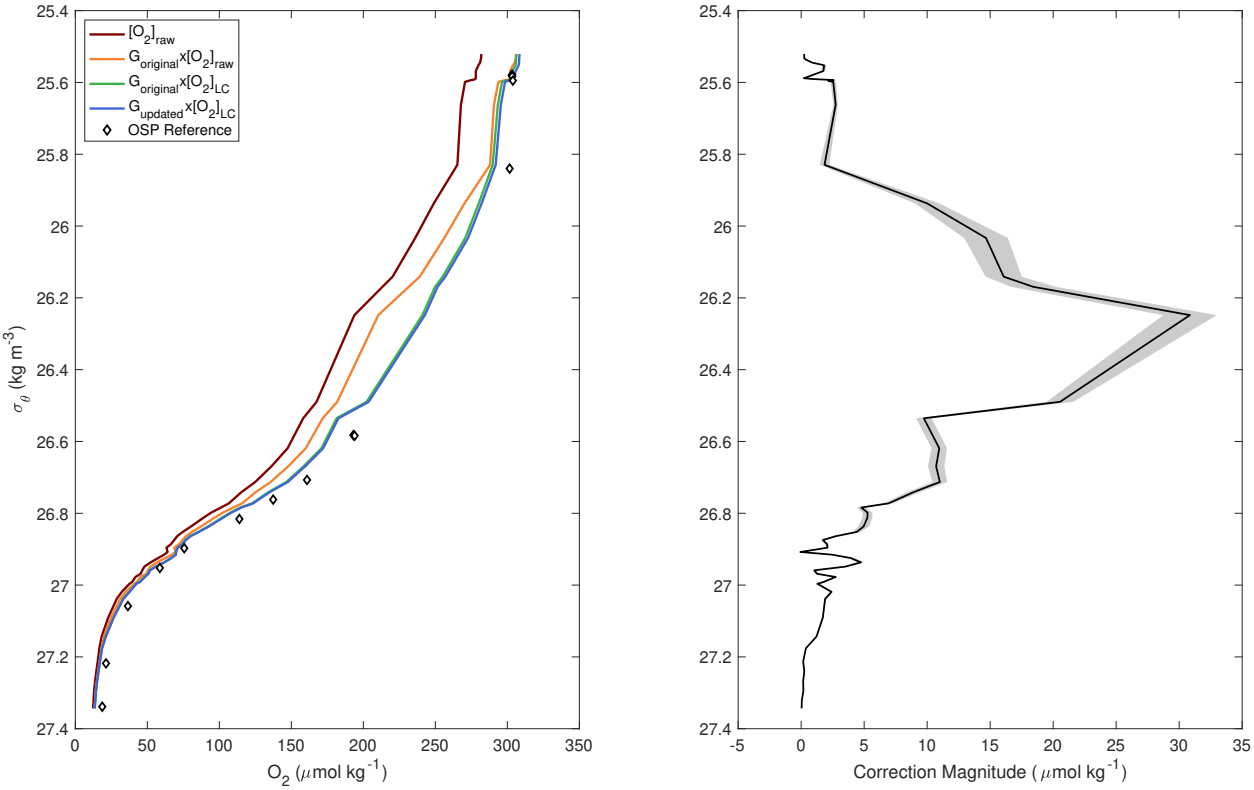

Figure A.5: Same as Figure 3.2 but for float # 5903274 on June 18, 2010. OSP reference profile is from June 13, 2010.

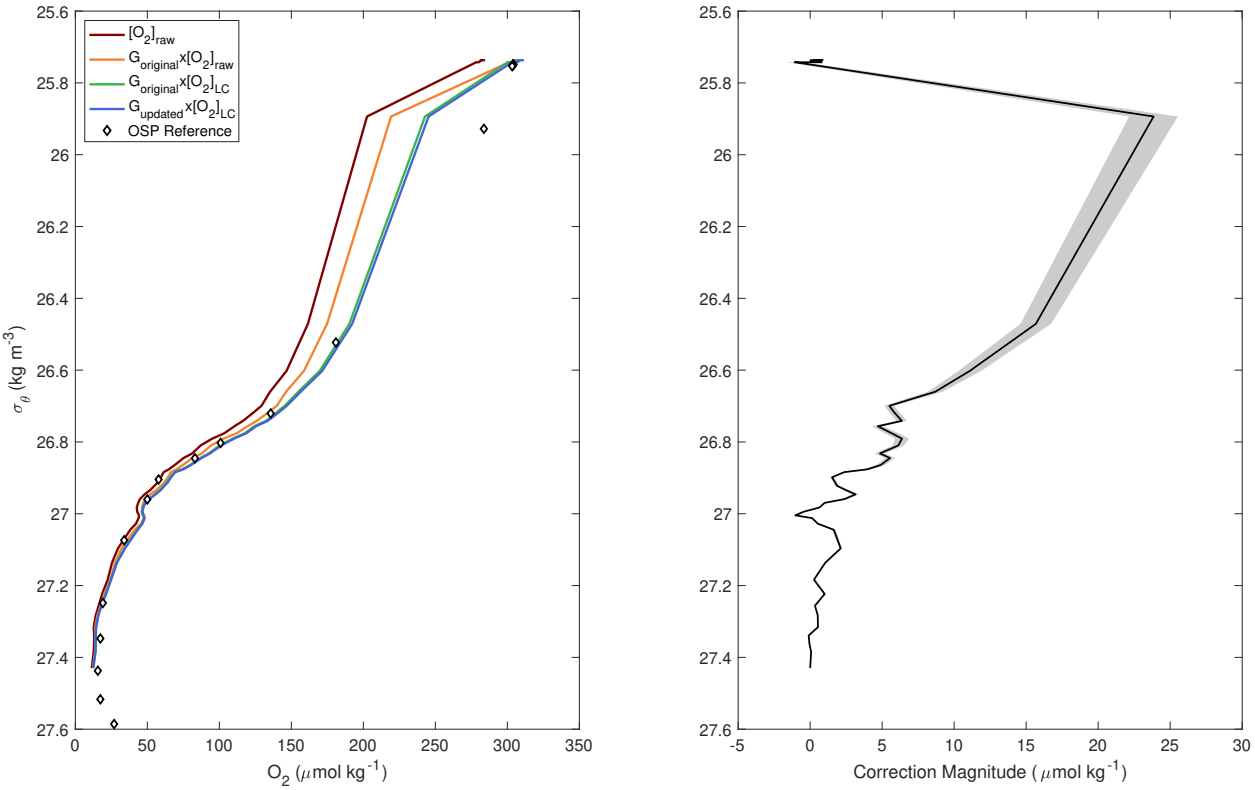

Figure A.6: Same as Figure 3.2 but for float # 5903274 on February 17, 2011. OSP reference profile is from February 15, 2011.

A.2.3 WMO# 5903405

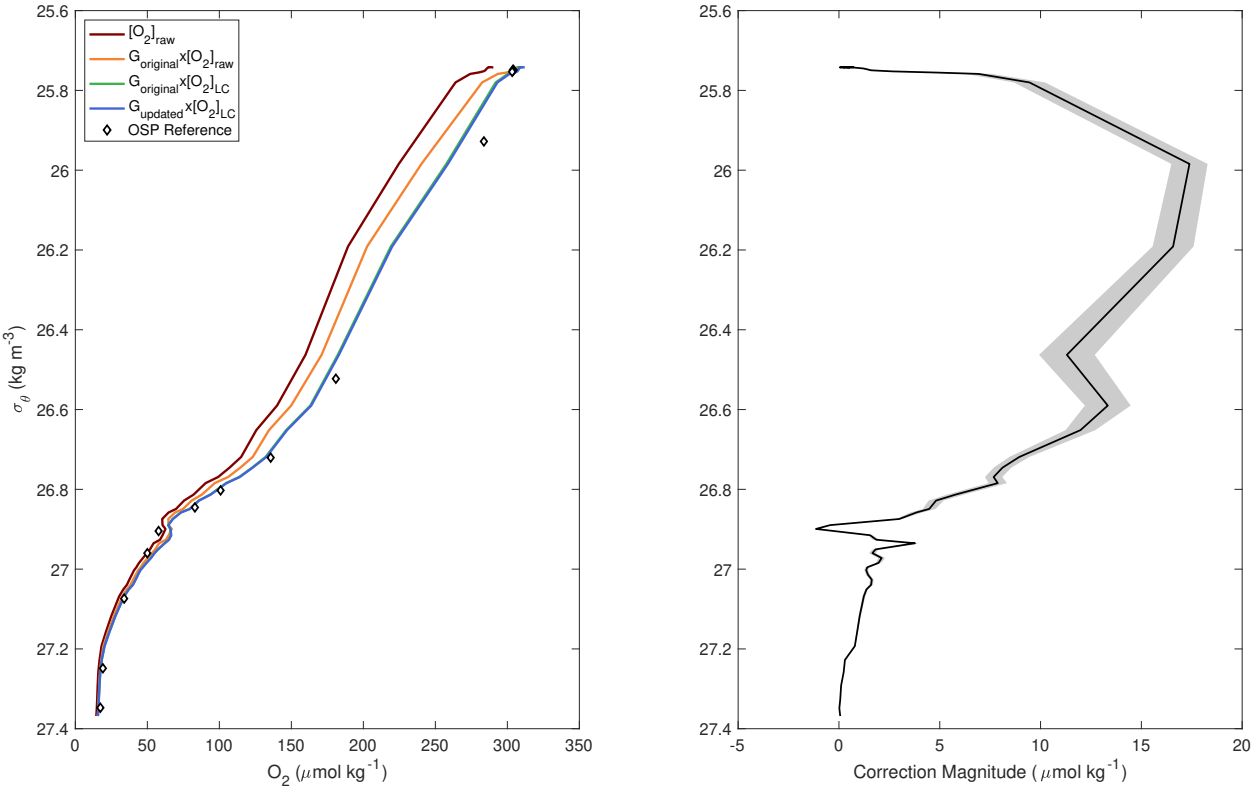

Figure A.7: Same as Figure 3.2 but for float # 5903405 on February 16, 2011. OSP reference profile is from February 15, 2011.

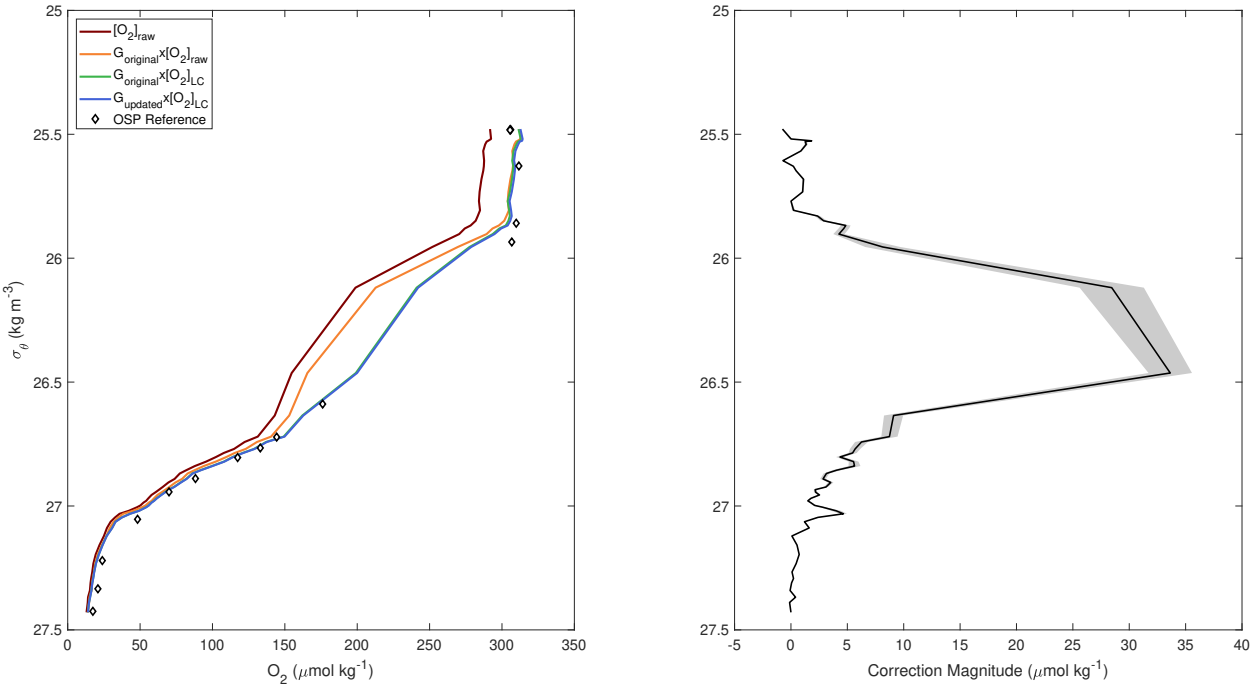

Figure A.8: Same as Figure 3.2 but for float # 5903405 on June 10, 2011. OSP reference profile is from June 12, 2011.

A.2.4 WMO# 5903714

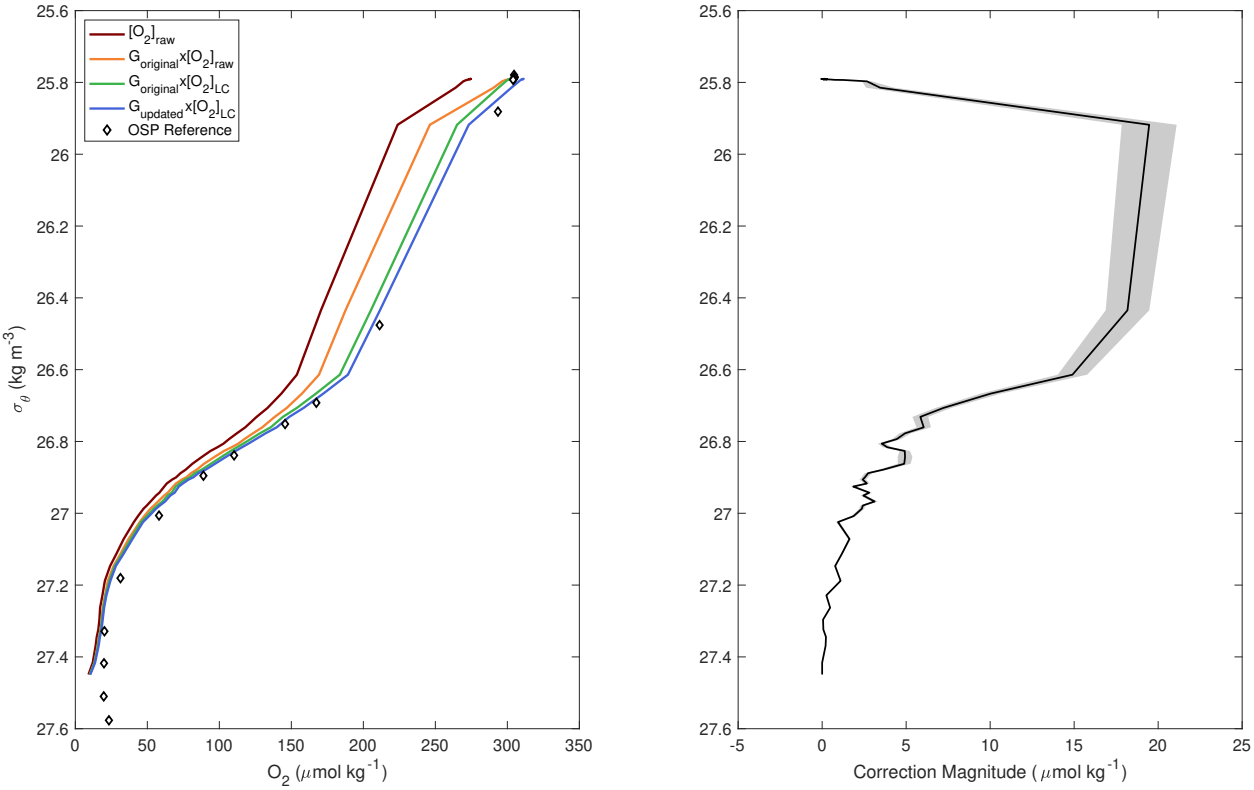

Figure A.9: Same as Figure 3.2 but for float # 5903714 on February 16, 2012. OSP reference profile is from February 15, 2012.

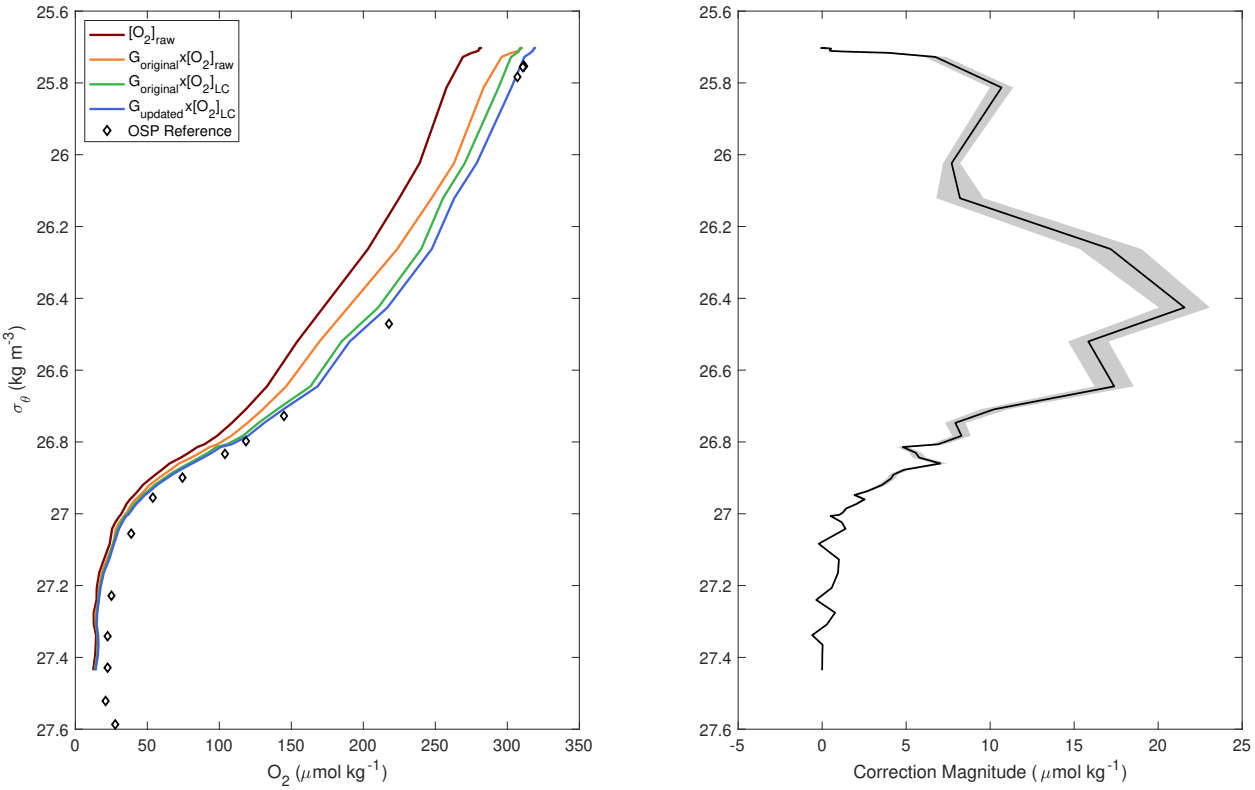

Figure A.10: Same as Figure 3.2 but for float # 5903714 on February 14, 2013. OSP reference profile is from February 12, 2013.

A.2.5 WMO# 5903743

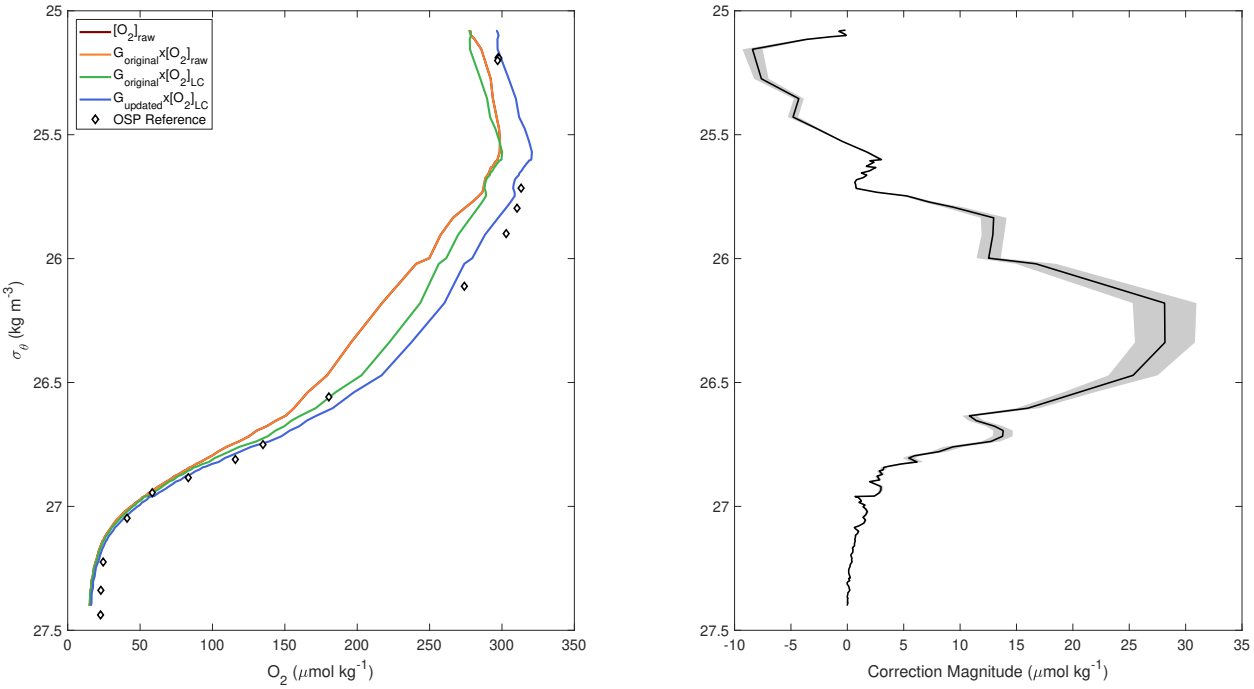

Figure A.11: Same as Figure 3.2 but for float # 5903743 on June 20, 2013. OSP reference profile is from June 17, 2013.

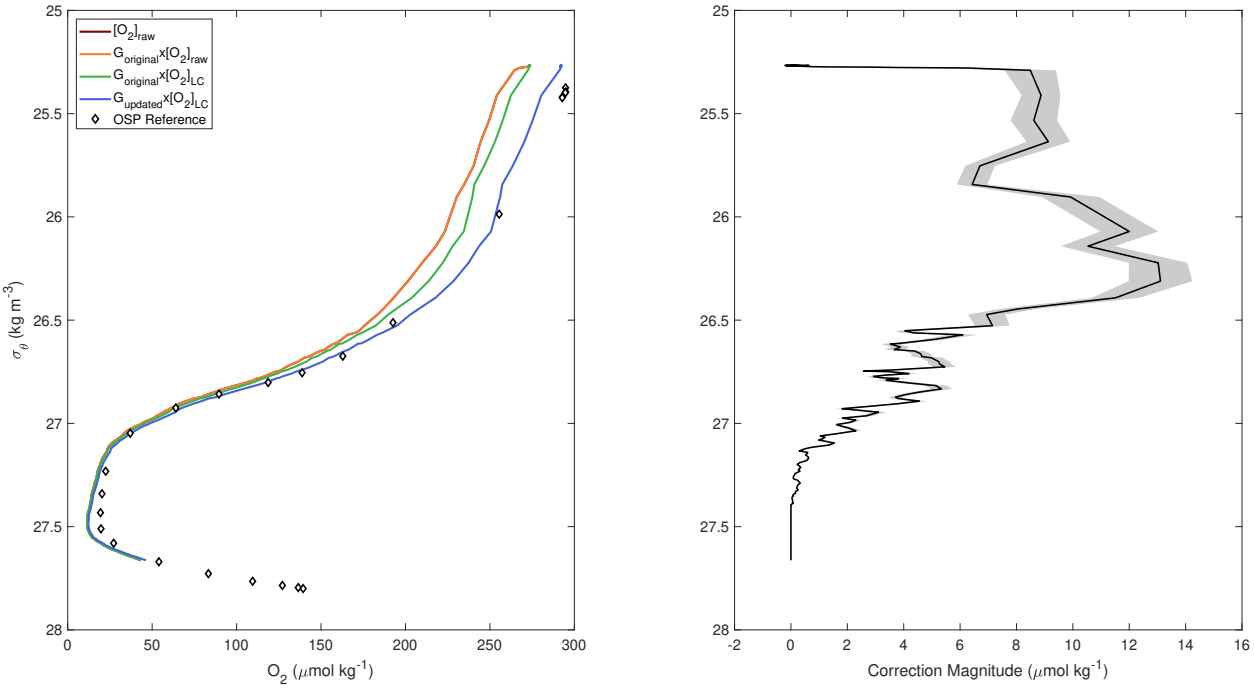

Figure A.12: Same as Figure 3.2 but for float # 5903743 on February 18, 2015. OSP reference profile is from February 18, 2015.

A.2.6 WMO# 5903891

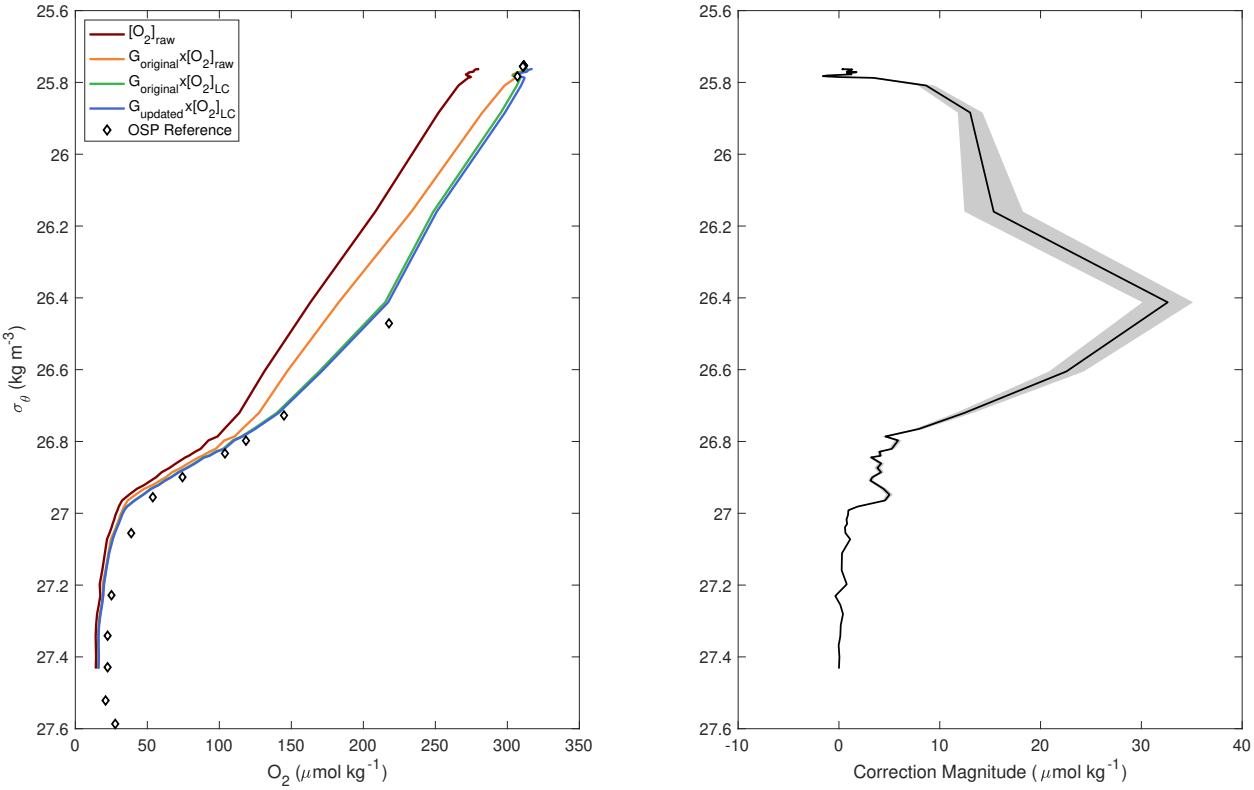

Figure A.13: Same as Figure 3.2 but for float # 5903891 on February 13, 2013. OSP reference profile is from February 12, 2013.

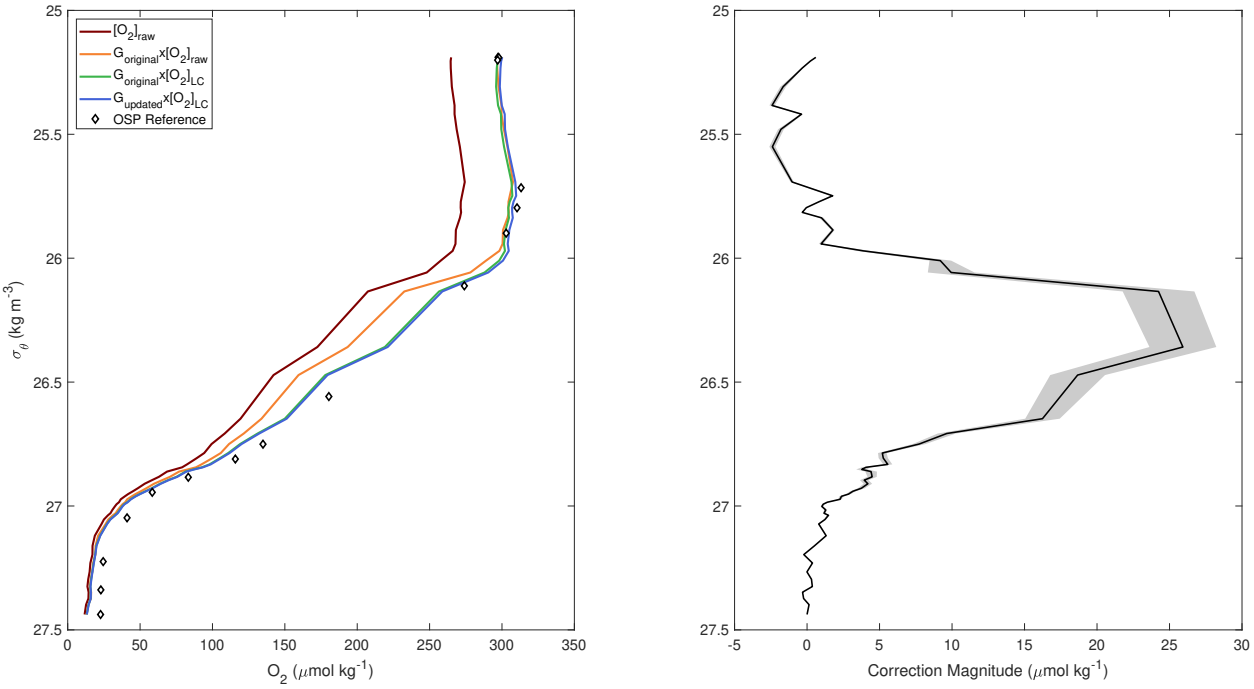

Figure A.14: Same as Figure 3.2 but for float # 5903891 on June 18, 2013. OSP reference profile is from June 17, 2013.

A.2.7 WMO# 5904095

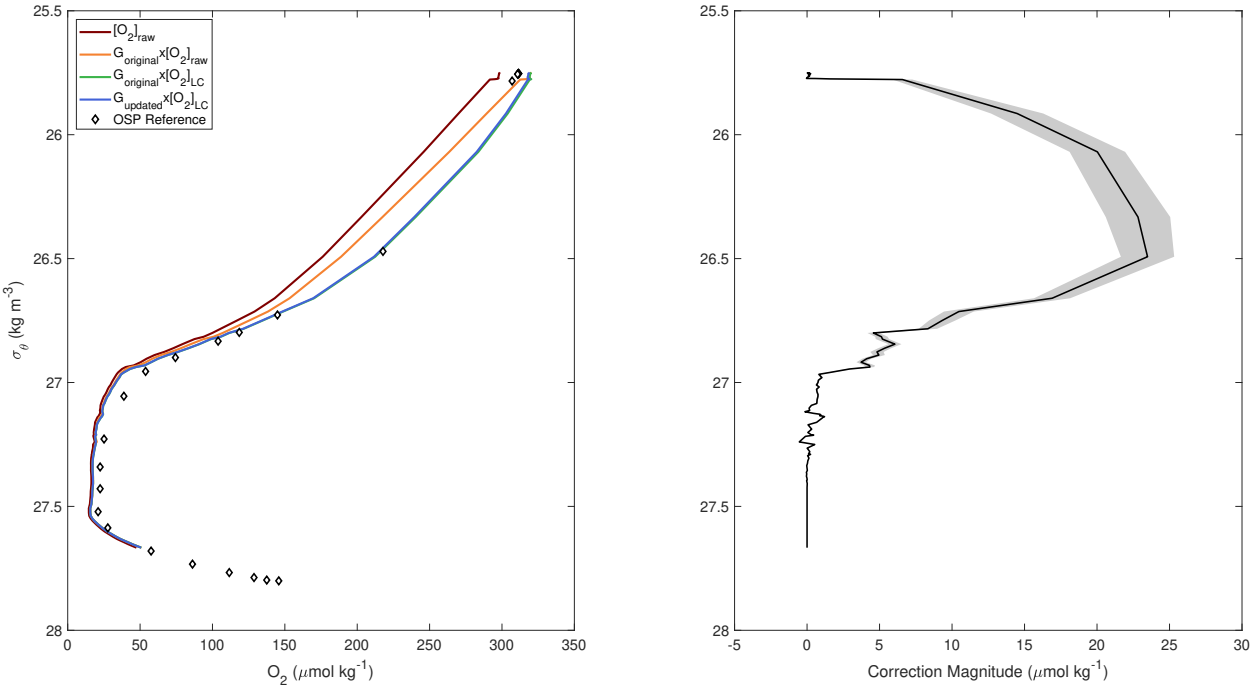

Figure A.15: Same as Figure 3.2 but for float # 5904095 on February 13, 2013. OSP reference profile is from February 12, 2013.

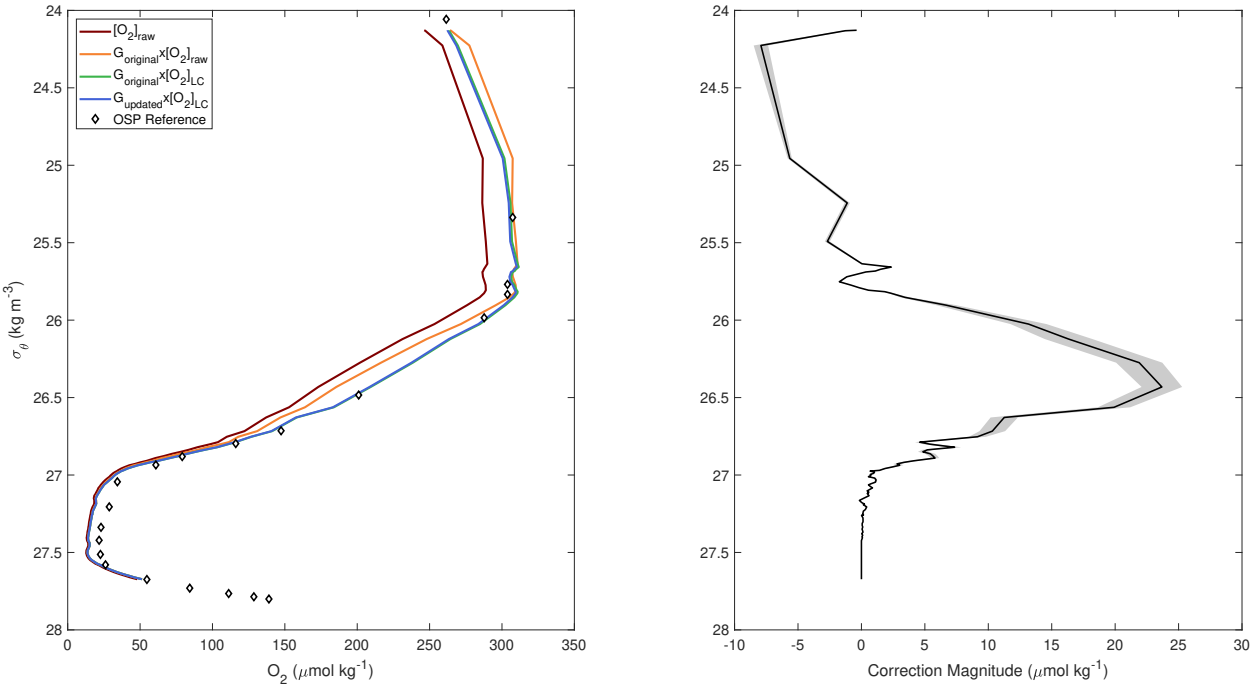

Figure A.16: Same as Figure 3.2 but for float # 5904095 on August 29, 2013. OSP reference profile is from August 31, 2013.

A.2.8 WMO# 5904125

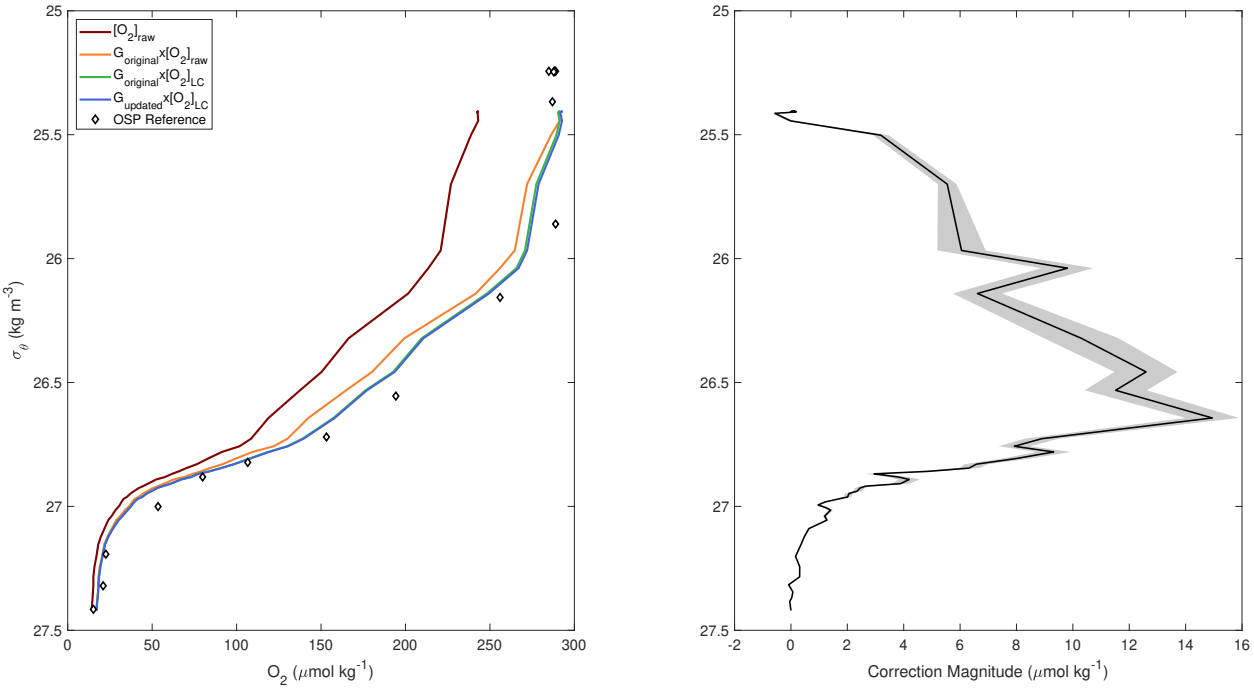

Figure A.17: Same as Figure 3.2 but for float # 5904125 on February 18, 2014. OSP reference profile is from February 19, 2014.

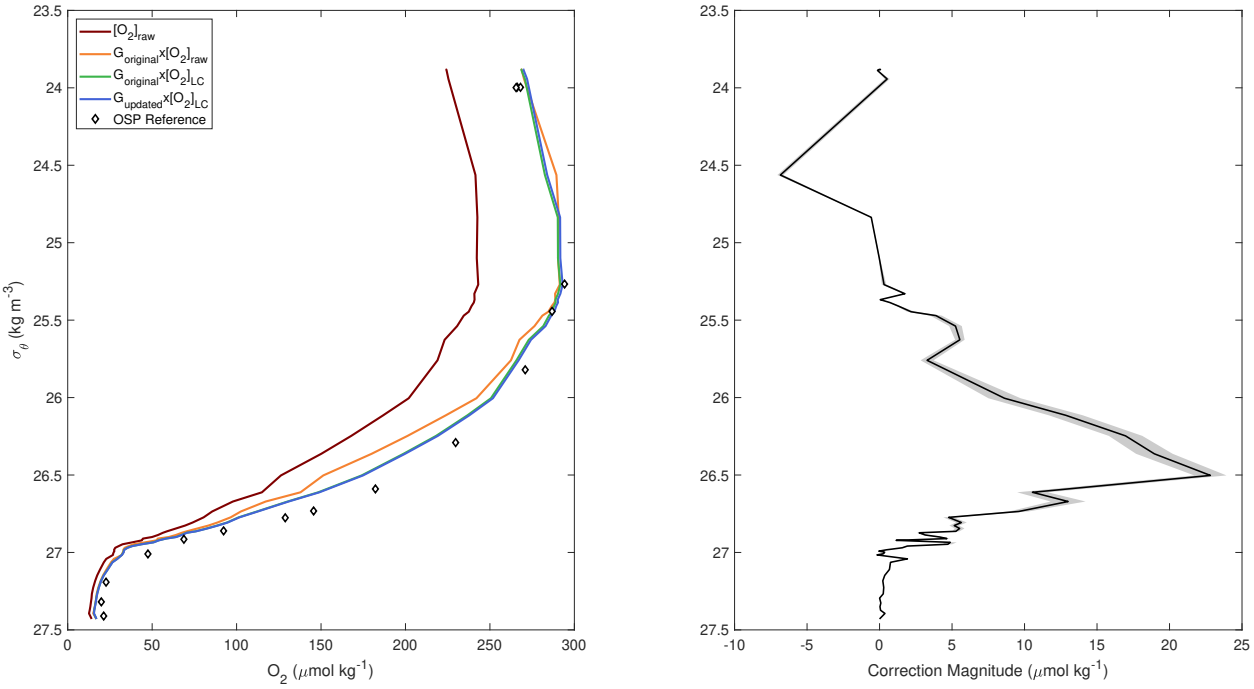

Figure A.18: Same as Figure 3.2 but for float # 5904125 on August 29, 2014. OSP reference profile is from August 28, 2014.

A.3 Deep Water O_2 Calibration

Wolf et al. (2018) successfully calibrated optodes on Argo floats in the Labrador Sea using the stable O_2 saturation in deeper waters. Based on their success, I attempted a similar calibration for the Argo floats in the subarctic Northeast Pacific. I calculated a "deep gain" to bring float O_2 saturation observations within the 27.49–27.53 σ_θ density range to the same mean value as the OSP observations (Figure A.19). However, applying this "deep gain" to the entire O_2 profile leads to large errors in surface O_2 concentrations (Figure A.20). This error is likely due to the low O_2 saturation within the density range used to calculate the "deep gain". D'Asaro and McNeil (2013) show that optode gain is non-linearly related to O_2 saturation (see their Figure 5). Calculating a gain in these low O_2 conditions therefore incorporates this non-linearity, resulting in the poor fit in the well-oxygenated surface waters. Deep convection in the Labrador Sea causes relatively stable O_2 saturations near 86% around 1800–1900 m, which likely explains the success of Wolf et al. (2018) in applying this method using deep water values.

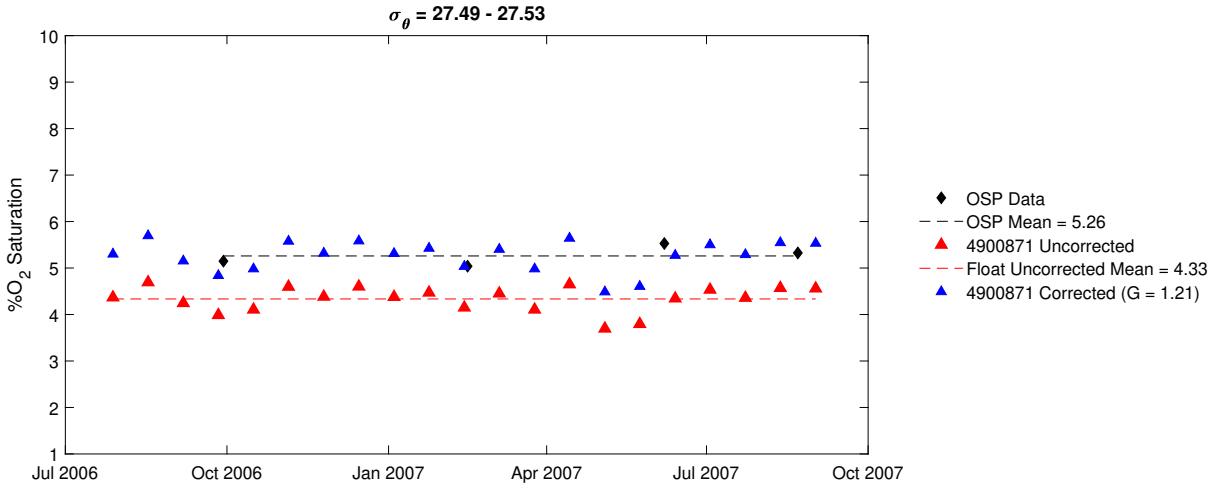

Figure A.19: O_2 saturation from OSP (black diamonds) and float (triangle) observations in the 27.49-27.53 σ_θ range. A "deep gain" was calculated as the value needed to adjust the mean uncorrected float O_2 saturation (red triangles) so that the mean corrected float O_2 saturation (blue triangles) matched the OSP mean value.

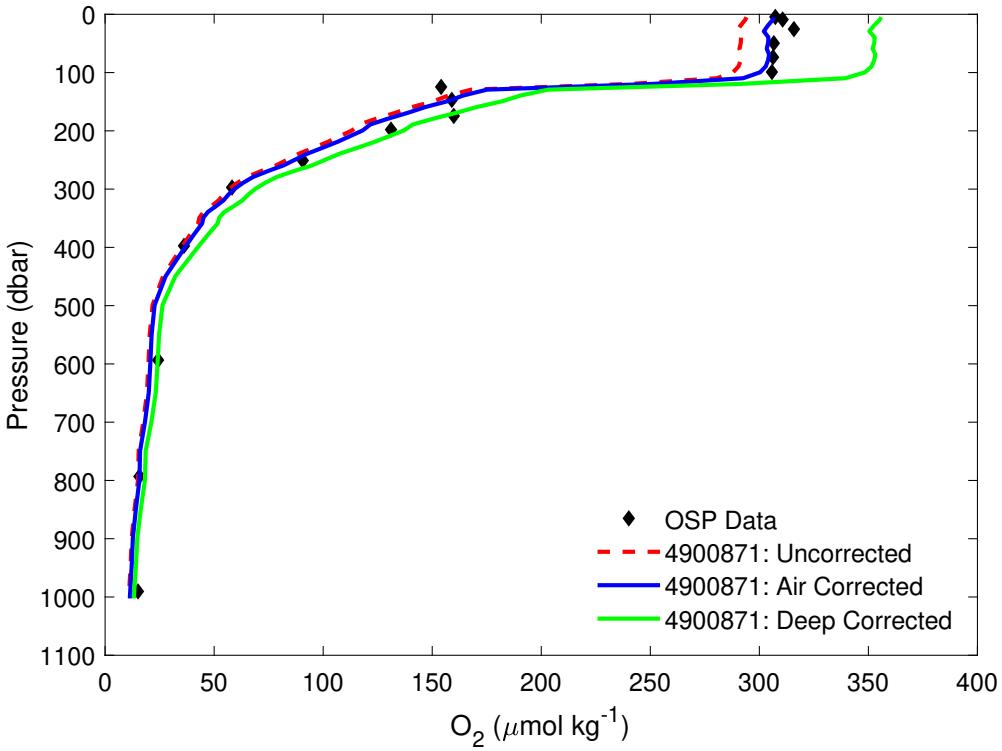

Figure A.20: An example O_2 profile for float 4900871 without no gain correction (red, dashed line), with in-air optode calibration (blue line), and the "deep gain" calibration (green line). The deep gain creates a large bias in surface O_2 measurements.

A.4 Optode Sensor Drift Analysis

The stability of the optimal profile gain for each float indicates that these floats experienced minimal drift during the time in which they remained in the study area. Individual gains were determined for each float profile within 10 days and 150 km of OSP following Section 3.2 (Figure A.21), and a trend line was fit to the individual gains. Since gain is a unitless scaling factor, the trend units are in yr^{-1}. Only three of the eight floats have a trend that is significantly different from 0 yr^{-1}, and the statistically significant trends are all <2% per year (Table A.1). Given these results, I chose not to apply a time-dependent gain to the floats in this study and instead apply the average gain to all O_2 observations for the float.

Table A.1: Trends in float gain over time with 95% confidence interval. If the confidence interval contains 0 yr^{-1}, trend is considered to be not statistically significant.

WMO #	Trend Best Estimate yr^{-1}	Lower 95% CI Bound yr^{-1}	Upper 95% CI Bound yr^{-1}
5902128	1.8 x 10^{-2}	4.9 x 10^{-3}	3.2 x 10^{-2}
5903274	1.9 x 10^{-2}	-4.6 x 10^{-2}	8.4 x10^{-2}
5903405	-8.5 x 10^{-2}	-5.1 x 10^{-2}	3.4 x10^{-2}
5903714	1.4 x 10^{-3}	-2.9 x 10^{-3}	3.2 x10^{-2}
5903743	1.6 x 10^{-2}	5.7 x 10^{-3}	2.5 x10^{-2}
5903891	5.3 x 10^{-2}	-1.9 x 10^{-1}	2.9 x10^{-1}
5904095	1.3 x 10^{-2}	2.2 x 10^{-3}	2.4 x 10^{-2}
5904125	-1.2 x 10^{-2}	-4.6 x 10^{-2}	2.2 x10^{-2}

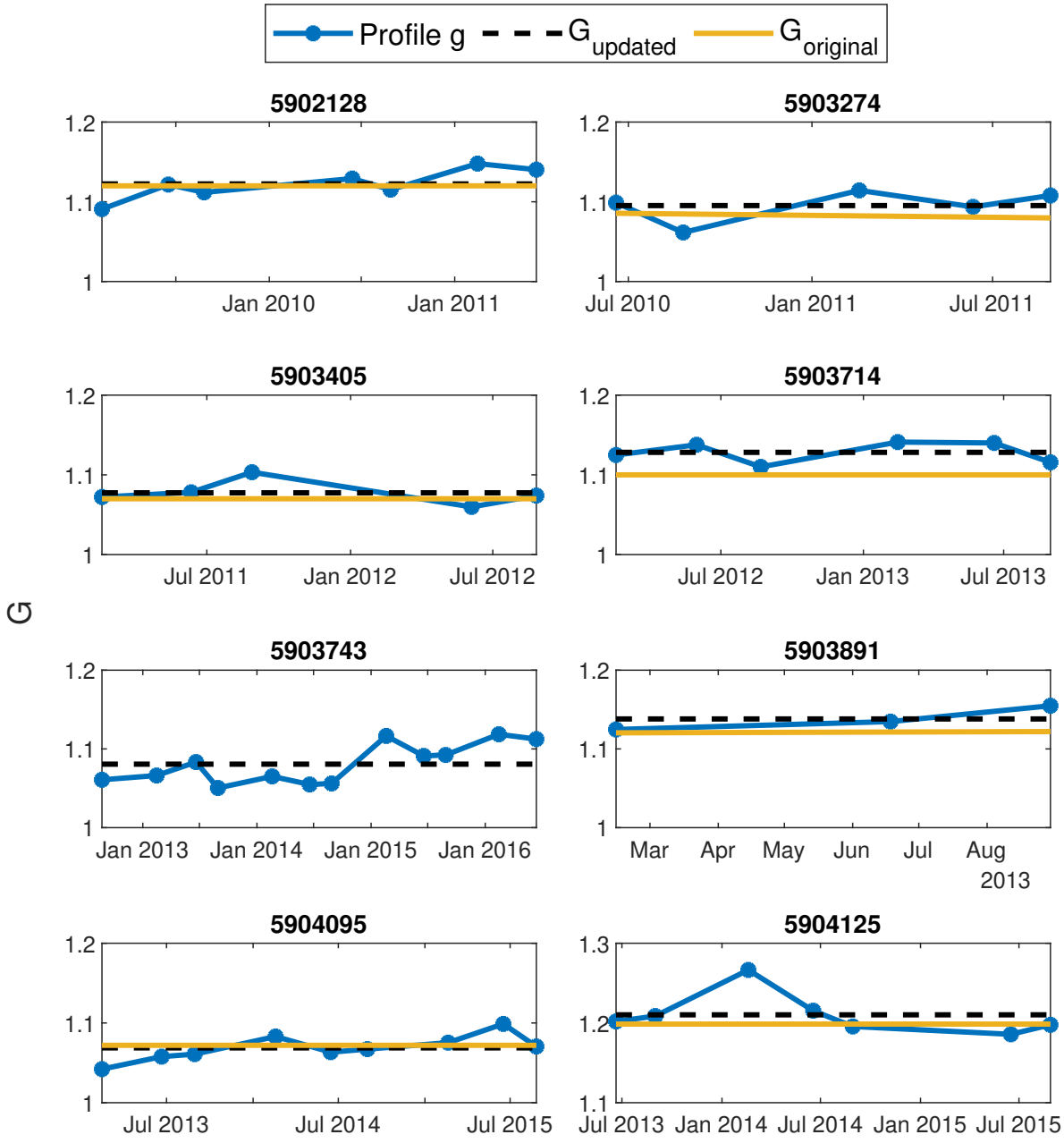

Figure A.21: Gains for each float on individual profiles within 10 days and 150 km of a discrete sample profile from OSP (profile g), the average of all profile g which is applied to the entire float ($G_{updated}$), and the previously applied gain from the Argo netCDF files ($G_{original}$). Note that float 5903743 did not have a $G_{original}$, and that the y-axis scale is different for float 5904125.

A.5 26.3 and 26.7 σ_θ Isopycnal Properties

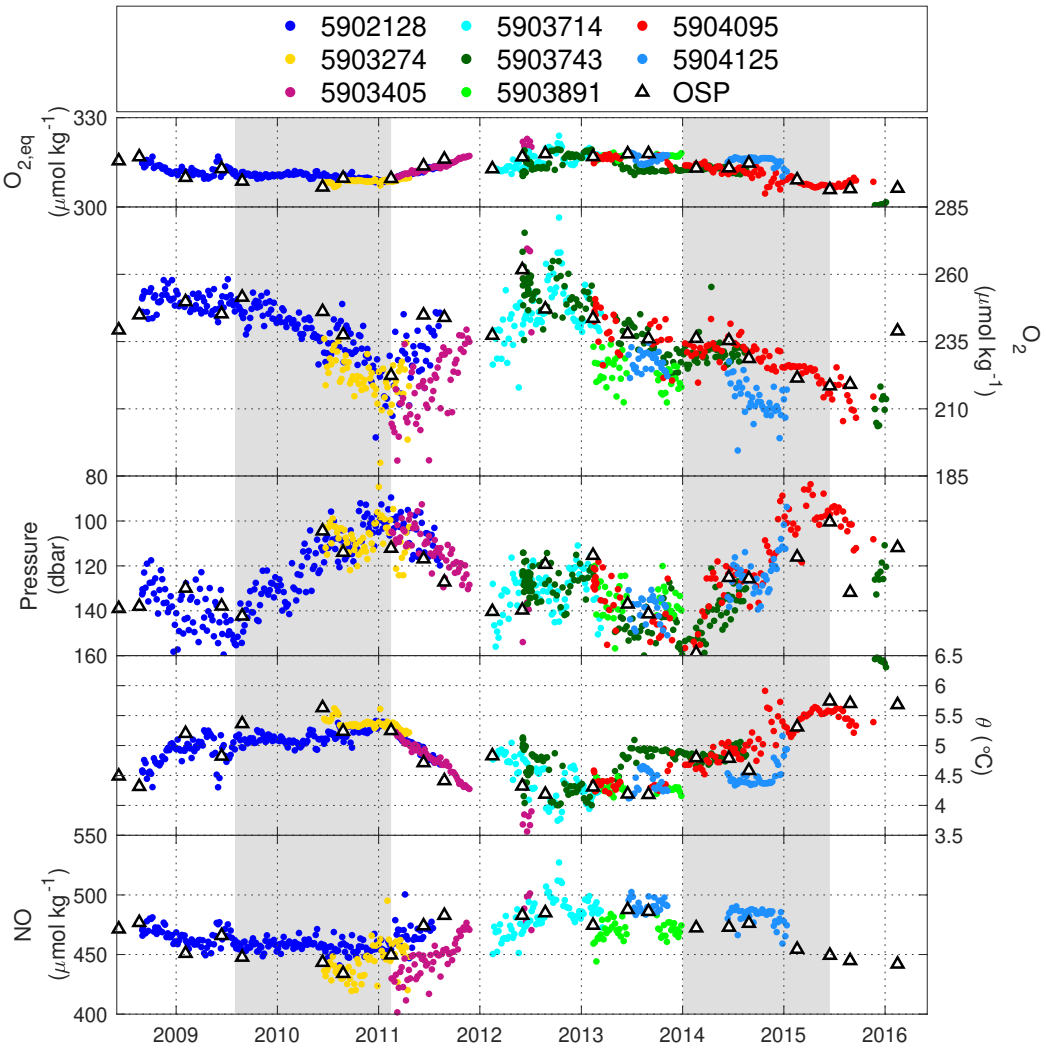

Figure A.22: Same as Figure 4.3 but for $\sigma_\theta = 26.3$.

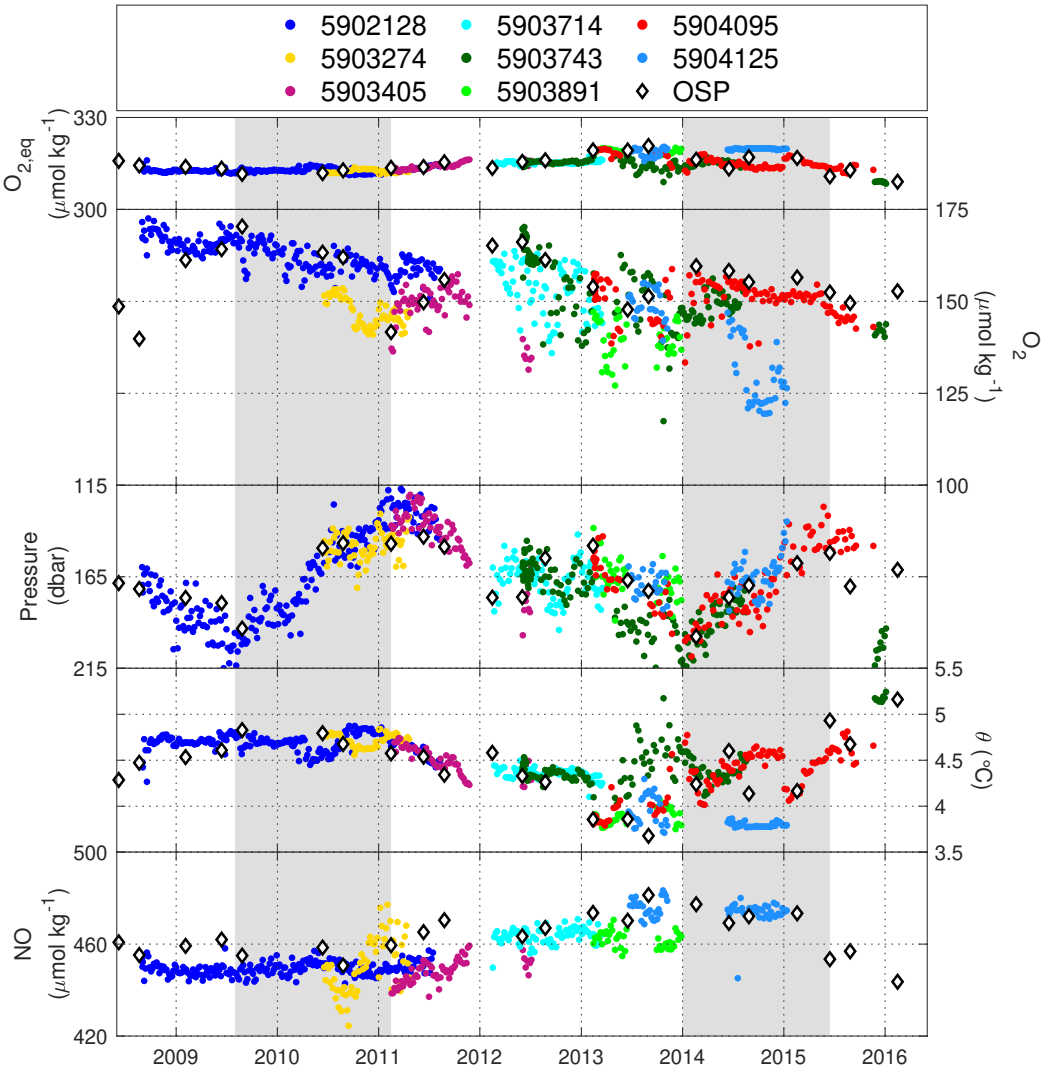

Figure A.23: Same as Figure 4.3 but for $\sigma_\theta = 26.7$.

A.6 33.65 g kg^{-1} Isohaline Properties

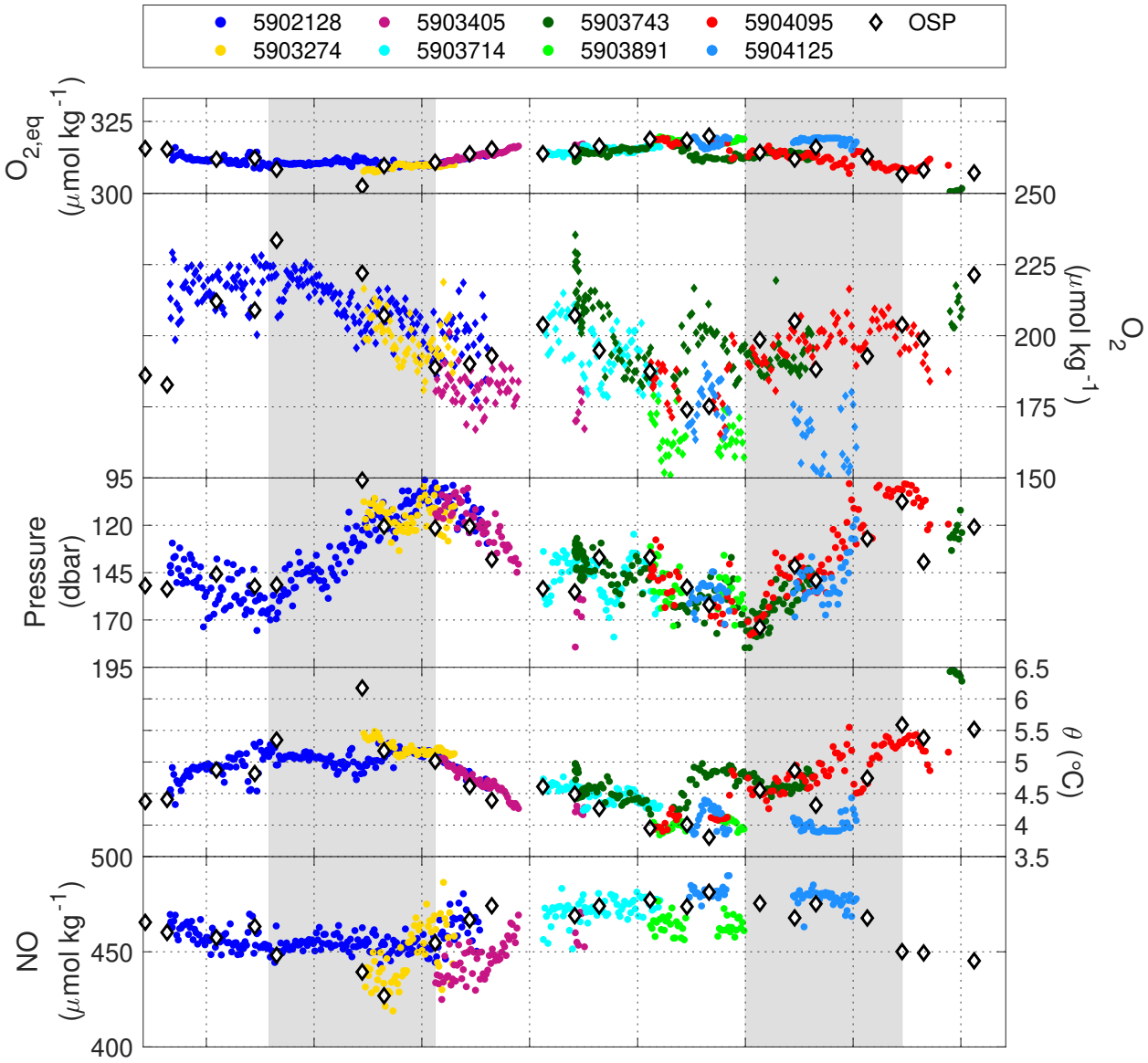

Figure A.24: Same as Figure 4.3 but for the 33.65 g kg^{-1} isohaline. This isohaline was chosen because 33.65 g kg^{-1}is approximately the average absolute salinity of the 26.5 σ_θ isopycnal.

References

Akima, H. (1970). A New Method of Interpolation and Smooth Curve Fitting Based on Local Procedures. *Journal of the Association for Computing Machinery*, *17*(1), 589–602. doi: 10.1145/321607.321609

Akima, H. (1974). A method of bivariate interpolation and smooth surface fitting based on local procedures. *Communications of the ACM*, *17*(1), 18–20. doi: 10.1145/360767.360779

Argo. (2021). *Argo float data and metadata from Global Data Assembly Centre (Argo GDAC) - Snapshot of Argo GDAC of February 10th 2021* [Dataset]. SEANOE. doi: 10.17882/42182#81474

Babbin, A. R., Bianchi, D., Jayakumar, A., & Ward, B. B. (2015). Rapid nitrous oxide cycling in the suboxic ocean. *Science*, *348*(6239), 1127–1129. doi: 10.1126/science.aaa8380

Bianchi, D., Dunne, J. P., Sarmiento, J. L., & Galbraith, E. D. (2012). Data-based estimates of suboxia, denitrification, and N2O production in the ocean and their sensitivities to dissolved O2. *Global Biogeochemical Cycles*, *26*. doi: 10.1029/2011GB004209

Bittig, H. C., Fiedler, B., Scholz, R., Krahmann, G., & Körtzinger, A. (2014). Time response of oxygen optodes on profiling platforms and its dependence on flow speed and temperature. *Limnology and Oceanography: Methods*, *12*, 617–636. doi: 10.4319/lom.2014.12.617

Bittig, H. C., & Körtzinger, A. (2017). Technical note: Update on response times, in-air measurements, and in situ drift for oxygen optodes on profiling platforms. *Ocean Science*, *13*(1), 1–11. doi: 10.5194/os-13-1-2017

Bittig, H. C., Körtzinger, A., Neill, C., van Ooijen, E., Plant, J. N., Hahn, J., ... Emerson, S. R. (2018). Oxygen optode sensors: Principle, characterization, calibration, and application in the ocean. *Frontiers in Marine Science*, *4*, 1–25. doi: 10.3389/fmars.2017.00429

Bond, N. A., Cronin, M. F., Freeland, H., & Mantua, N. (2015). Causes and impacts of the 2014 warm anomaly in the NE Pacific. *Geophysical Research Letters*, *42*(9), 3414–3420. doi: 10.1002/2015GL063306

Boyer, T., Garcia, H., Locarnini, R., Zweng, M., Mishonov, A., Reagan, J., ... Smolyar, I. (2018). *World Ocean Atlas 2018* [Dataset]. NOAA National Centers for Environmental Information. Retrieved June 24, 2021, from `https://www.ncei.noaa.gov/archive/accession/NCEI-WOA18`

Broecker, W. S. (1974). "NO", A Conservative Water-Mass Tracer. *Earth and Planetary*

Science Letters, *23*, 100–107. doi: 10.1016/0012-821X(74)90036-3

Buesseler, K. O., Benitez-Nelson, C. R., Roca-Martí, M., Wyatt, A. M., Resplandy, L., Clevenger, S. J., ... Umhau, B. P. (2020). High-resolution spatial and temporal measurements of particulate organic carbon flux using thorium-234 in the northeast Pacific Ocean during the export processes in the ocean from remote sensing field campaign. *Elementa*, *8*(1), 1–19. doi: 10.1525/elementa.2020.030

Carpenter, J. H. (1965). The Accuracy of the Winkler Method for Dissolved Oxygen Analysis. *Limnology and Oceanography*, *10*(1), 135–140. doi: 10.4319/lo.1965.10.1.0135

Crawford, W. R., & Peña, M. A. (2016). Decadal trends in oxygen concentration in subsurface waters of the Northeast Pacific Ocean. *Atmosphere - Ocean*, *54*(2), 171–192. doi: 10.1080/07055900.2016.1158145

Culberson, C. (1991). Dissolved Oxygen [WOCE]. In *WOCE Operations Manual. Volume 3: The Observational Program. Section 3.1: WOCE Hydrographic Program. Part 3.1.3: WHP Operations and Methods. WHP Office Report WHPO 91-1/WOCE Report No. 68/91.*

Cummins, P. F., & Lagerloef, G. S. (2002). Low-frequency pycnocline depth variability at Ocean Weather Station P in the northeast Pacific. *Journal of Physical Oceanography*, *32*(11), 3207–3215. doi: 10.1175/1520-0485(2002)032<3207:LFPDVA>2.0.CO;2

Cummins, P. F., & Masson, D. (2012). Wind-driven variability of dissolved oxygen below the mixed layer at Station P. *Journal of Geophysical Research: Oceans*, *117*(8), 1–9. doi: 10.1029/2011JC007847

Cummins, P. F., & Masson, D. (2018). Low-frequency isopycnal variability in the Alaska Gyre from Argo. *Progress in Oceanography*, *168*, 310–324. doi: 10.1016/j.pocean.2018.09.014

Cummins, P. F., & Ross, T. (2020). Secular trends in water properties at Station P in the northeast Pacific: An updated analysis. *Progress in Oceanography*, *186*, 102329. doi: 10.1016/j.pocean.2020.102329

D'Asaro, E., & McNeil, C. (2013). Calibration and Stability of Oxygen Sensors on Autonomous Floats. *Journal of Atmospheric and Oceanic Technology*, *30*, 1896-1906. doi: 10.1175/JTECH-D-12-00222.1

Deutsch, C., Ferrel, A., Seibel, B., Pörtner, H.-O., & Huey, R. B. (2015). Climate change tightens a metabolic constraint on marine habitats. *Science*, *348*(6239), 1132–1135. doi: 10.1126/science.aaa1605

Drucker, R., & Riser, S. C. (2016). In situ phase-domain calibration of oxygen Optodes on profiling floats. *Methods in Oceanography*, *17*, 296–318. doi: 10.1016/j.mio.2016.09.007

Estapa, M., Buesseler, K., Durkin, C., Omand, M., Benitez-Nelson, C., Roca-Marti, M., ... Pike, S. (2020). Biogenic sinking particle fluxes at Ocean Station Papa. *Elementa Science of the Anthropocene*, *9*. doi: 10.1525/elementa.2020.00122

Fassbender, A., Bourbonnais, A., Clayton, S., Gaube, P., Omand, M., Franks, P., ... McGillicuddy Jr., D. (2018). "Interpreting mosaics of ocean biogeochemistry". *EOS*, *99*. doi: 10.1029/2018EO109707

Franco, A., Ianson, D., Ross, T., Hamme, R., A.H., M., J.R., C., ... Tortell, P. (2021). Anthropogenic and Climatic Contributions to Observed Carbon System Trends in the Northeast Pacific. *Global Biogeochemical Cycles*, *35*(7). doi: 10.1029/2020GB006829

Freeland, H., & Cummins, P. (2005). Argo: A new tool for environmental monitoring and assessment of the world's oceans, an example from the N.E. Pacific. *Progress in Oceanography*, *64*(1), 31–44. doi: 10.1016/j.pocean.2004.11.002

Garcia, H., Weathers, K., Paver, C., Smolyar, I., Boyer, T., Locarnini, R., ... Reagan, J. (2019). *World Ocean Atlas 2018, Volume 3: Dissolved Oxygen, Apparent Oxygen Utilization, and Dissolved Oxygen Saturation* (NOAA Atlas NESDIS No. 83).

Gordon, C., Fennel, K., Richards, C., Shay, L. K., & Brewster, J. K. (2020). Can ocean community production and respiration be determined by measuring high-frequency oxygen profiles from autonomous floats? *Biogeosciences*, *17*, 4119–4134. doi: 10.5194/bg-17-4119-2020

Haskell, W. Z., Fassbender, A. J., Long, J. S., & Plant, J. N. (2020). Annual Net Community Production of Particulate and Dissolved Organic Carbon From a Decade of Biogeochemical Profiling Float Observations in the Northeast Pacific. *Global Biogeochemical Cycles*, *34*(10), 1–22. doi: 10.1029/2020GB006599

IOC, SCOR, & IAPSO. (2010). *The International Thermodynamic Equation of Seawater – 2010: Calculation and use of thermodynamic properties* (Intergovernmental Oceanographic Commission, Manuals and Guides No. 56).

Ito, T., Minobe, S., Long, M. C., & Deutsch, C. (2017). Upper ocean O2 trends: 1958–2015. *Geophysical Research Letters*, *44*(9), 4214–4223. doi: 10.1002/2017GL073613

Johnson, K., Bif, M., Bushinsky, S., Fassbender, A., & Takeshita, Y. (2020). Biogeochemical Argo [in "State of the Climate in 2019"]. *Bulletin of the American Meteorological Society*, *101*(8), S167-S169. doi: 10.1175/BAMS-D-20-0105.1

Johnson, K., Plant, J. N., Riser, S. C., & Gilbert, D. (2015). Air oxygen calibration of oxygen optodes on a profiling float array. *Journal of Atmospheric and Oceanic Technology*, *32*(11), 2160–2172. doi: 10.1175/JTECH-D-15-0101.1

Kako, S., & Kubota, M. (2007). Variability of mixed layer depth in Kuroshio/Oyashio Extension region: 2005-2006. *Geophysical Research Letters*, *34*, 2005–2006. doi:

10.1029/2007GL030362

Locarnini, R., Boyer, T., Mishonov, A., Reagan, J., Zweng, M., Baranova, O., ... Smolyar, I. (2019). *World Ocean Atlas 2018, Volume 5: Density* (NOAA Atlas NESDIS No. 85).

Mackinson, B., Moran, S., Lomas, M., Steward, G., & Kelly, R. (2015). Estimates of micro-, nano-, and picoplankton contributions to particle export in the northeast Pacific. *Biogeosciences*, *12*, 3429-3446. doi: 10.5194/bg-12-3429-2015

Martin, J. H., Knauer, G. A., Karl, D. M., & Broenkow, W. W. (1987). VERTEX: carbon cycling in the northeast Pacific. *Deep Sea Research Part A, Oceanographic Research Papers*, *34*(2), 267–285. doi: 10.1016/0198-0149(87)90086-0

Mccormick, L. R., & Levin, L. A. (2017). Physiological and ecological implications of ocean deoxygenation for vision in marine organisms. *Philosophical Transactions of the Royal Society A*, *375*(2102). doi: 10.1098/rsta.2016.0322

Mecking, S., Warner, M., & Bullister, J. (2006). Temporal changes in pcfc-12 ages and aou along two hydrographic sections in the eastern subtropical north pacific. *Deep Sea Research Part 1: Oceanographic Research Papers*, *53*(1). doi: 10.1016/j.dsr.2005.06.018

Onishi, H. (2001). Spatial and temporal variability in a vertical section across the Alaskan stream and subarctic current. *Journal of Oceanography*, *57*(1), 79–91. doi: 10.1023/A:1011178821299

Ono, T., Midorikawa, T., Watanabe, Y., Tadokoro, K., & Saino, T. (2001). Temporal increases of phosphate and apparent oxygen utilization in the subsurface waters of western subarctic pacific from 1968 to 1998. *Geophysical Research Letters*, *28*(17). doi: 10.1029/2001GL012948

Oschlies, A., Brandt, P., Stramma, L., & Schmidtko, S. (2018). Drivers and mechanisms of ocean deoxygenation. *Nature Geoscience*, *11*(7), 467–473. doi: 10.1038/s41561-018-0152-2

Pelland, N. A., Eriksen, C. C., & Cronin, M. F. (2016). Seaglider surveys at Ocean Station Papa: Circulation and water mass properties in a meander of the North Pacific Current. *Journal of Geophysical Research: Oceans*, *121*, 6816–6846. doi: 10.102/2016JC011920

Plant, J. N., Johnson, K. S., Sakamoto, C. M., Jannasch, H. W., Coletti, L. J., Riser, S. C., & Swift, D. D. (2016). Net community production at Ocean Station Papa observed with nitrate and oxygen sensors on profiling floats. *Global Biogeochemical Cycles*, *30*, 859–879. doi: 10.1002/2015GB005349

Robinson, C. (2019). Microbial Respiration, the Engine of Ocean Deoxygenation. *Frontiers in Marine Science*, *5*. doi: 10.3389/fmars.2018.00533

Roemmich, E., & Gilson, J. (2009). The 2004-2008 mean and annual cycle of temperature, salinity, and steric height in the global ocean from the Argo Program. *Progress in*

Oceanography, *82*(2), 81–100. doi: 10.1016/j.pocean.2009.03.004

Ross, T., Du Preez, C., & Ianson, D. (2020). Rapid deep ocean deoxygenation and acidification threaten life on Northeast Pacific seamounts. *Global Change Biology*, *26*(11), 6424–6444. doi: 10.1111/gcb.15307

Scannell, H., Johnson, G., Thompson, L., Lyman, J., & Riser, S. (2020). Subsurface Evolution and Persistence of Marine Heatwaves in the Northeast Pacific. *Geophysical Research Letters*, *47*. doi: 10.1029/2020GL090548

Schmechtig, C., Thierry, V., & the Bio-Argo Team. (2016). *Argo Quality Control Manual for Biogeochemical Data, v1.0* (Tech. Rep.).

Schmidtko, S., Stramma, L., & Visbeck, M. (2017). Decline in global oceanic oxygen content during the past five decades. *Nature*, *542*(7641), 335–339. doi: 10.1038/nature21399

Takeshita, Y., Martz, T. R., Johnson, K. S., Plant, J. N., Gilbert, D., Riser, S. C., ... Tilbrook, B. (2013). A climatology-based quality control procedure for profiling float oxygen data. *Journal of Geophysical Research: Oceans*, *118*(10), 5640–5650.

Talley, L., Pickard, G., Emery, W., & Swift, J. (2011). *Descriptive Physical Oceanography: An Introduction*. Academic Press.

Thierry, V., Bittig, H., & the Argo-BGC Team. (2021). *Argo quality control manual for dissolved oxygen concentration, v2.1* (Tech. Rep.). doi: 10.13155/46542

Thomson, R. (1981). *Oceanography of the British Columbia coast* (Tech. Rep. No. 56).

Thomson, R., & Krassovski, M. (2010). Poleward reach of the California Undercurrent extension. *Journal of Geophysical Research*, *115*(C9). doi: 10.1029/2010JC006280

Ueno, H., & Yasuda, I. (2003). Intermediate water circulation in the North Pacific subarctic and northern subtropical regions. , *108*, 1–14. doi: 10.1029/2002JC001372

Watson, A. J., Lenton, T. M., & Mills, B. J. W. (2017). Ocean deoxygenation, the global phosphorus cycle and the possibility of ocean anoxia. *Philosophical Transactions of the Royal Society A*, *375*(2102). doi: 10.1098/rsta.2016.0318

Whitney, F. A. (2015). Anomalous winter winds decrease 2014 transition zone productivity in the NE Pacific. *Geophysical Research Letters*, *42*(2), 428–431. doi: 10.1002/2014GL062634

Whitney, F. A., Freeland, H. J., & Robert, M. (2007). Persistently declining oxygen levels in the interior waters of the eastern subarctic Pacific. *Progress in Oceanography*, *75*(2), 179–199. doi: 10.1016/j.pocean.2007.08.007

Wolf, M. K., Hamme, R. C., Gilbert, D., Yashayaev, I., & Thierry, V. (2018). Oxygen Saturation Surrounding Deep Water Formation Events in the Labrador Sea From Argo-O2 Data. *Global Biogeochemical Cycles*, *32*, 635–653. doi: 10.1002/2017GB005829

Wong, A., Keeley, R., Carval, T., & the Argo Data Management Team. (2021). *Argo Quality*

Control Manual For CTD and Trajectory Data, v3.5 (Tech. Rep.).

Wong, C., Waser, N., Whitney, F., Johnson, W., & Page, J. (2002). Time-series study of the biogeochemistry of the North East subarctic Pacific: reconciliation of the Corg/N remineralization and uptake ratios with the Redfield ratios. *Deep Sea Research Part II*, *49*, 5717-5738. doi: 10.1016/S0967-0645(02)00211-4

Yang, B., Emerson, S. R., & Angelica Penã, M. (2018). The effect of the 2013-2016 high temperature anomaly in the subarctic Northeast Pacific (the "blob") on net community production. *Biogeosciences*, *15*(21), 6747–6759. doi: 10.5194/bg-15-6747-2018